Available online at www.sciencedirect.com

ScienceDirect

Geochimica et Cosmochimica Acta 197 (2017) 378–395

Geochimica et Cosmochimica Acta

www.elsevier.com/locate/gca

Immiscible silicate liquids and phosphoran olivine in Netschaëvo IIE silicate: Analogue for planetesimal core–mantle boundaries

Nadia Van Roosbroek [a,b], Christopher Hamann [c,d,*], Seann McKibbin [b], Ansgar Greshake [c], Richard Wirth [e], Lidia Pittarello [b], Lutz Hecht [c,d], Philippe Claeys [b], Vinciane Debaille [a]

[a] *Laboratoire G-Time, DGES, Université Libre de Bruxelles, CP 160/02, 50 Avenue F. D. Roosevelt, B-1050 Brussels, Belgium*
[b] *Analytical, Environmental and Geo-Chemistry (AMGC), Vrije Universiteit Brussel, Pleinlaan 2, B-1050 Brussels, Belgium*
[c] *Museum für Naturkunde, Leibniz-Institut für Evolutions- und Biodiversitätsforschung, Invalidenstraße 43, D-10115 Berlin, Germany*
[d] *Institut für Geologische Wissenschaften, Freie Universität Berlin, Malteserstraße 74–100, D-12249 Berlin, Germany*
[e] *GeoForschungsZentrum Potsdam, Telegrafenberg, D-14473 Potsdam, Germany*

Received 28 January 2016; accepted in revised form 27 October 2016; available online 2 November 2016

Abstract

We have investigated a piece of the Netschaëvo IIE iron meteorite containing a silicate inclusion by means of electron microprobe analysis (EMPA) and transmission electron microscopy (TEM). Netschaëvo contains chondrule-bearing clasts and impact melt rock clasts were also recently found. The examined inclusion belongs to the latter and is characterized by a porphyritic texture dominated by clusters of coarse-grained olivine and pyroxene, set in a fine-grained groundmass that consists of new crystals of olivine and a hyaline matrix. This matrix material has a quasi-basaltic composition in the inner part of the inclusion, whereas the edge of the inclusion has a lower SiO_2 concentration and is enriched in MgO, P_2O_5, CaO, and FeO. Close to the metal host, the inclusion also contains euhedral Mg-chromite crystals and small (<2 μm), Si-rich globules. A TEM foil was cut from this glassy, silico-phosphate material. It shows that the material consists of elongated olivine crystallites containing up to 14 wt% P_2O_5, amorphous material, and interstitial Cl-apatite crystals. The Si-rich silicate glass globules show a second population of Fe-rich silicate glass droplets, indicating they formed by silicate liquid immiscibility. Together with the presence of phosphoran olivine and quenched Cl-apatite, these textures suggest rapid cooling and quenching as a consequence of an impact event. Moreover, the enrichment of phosphorus in the silicate inclusion close to the metal host (phosphoran olivine and Cl-apatite) indicates that phosphorus re-partitioned from the metal into the silicate phase upon cooling. This probably also took place in pallasite meteorites that contain late-crystallizing phases rich in phosphorus. Accordingly, our findings suggest that oxidation of phosphorus might be a general process in core–mantle environments, bearing on our understanding of planetesimal evolution. Thus, the Netschaëvo sample serves as a natural planetesimal core–mantle boundary experiment and based on our temperature estimates, the following sequence of events takes place: (i) precipitation of olivine (1400–1360 °C), (ii) re-partitioning of phosphorus from the metal into the silicate phase, and (iii) formation of immiscible melts (1230–1115 °C).
© 2016 Elsevier Ltd. All rights reserved.

Keywords: Iron meteorites; Impact melting; Netschaëvo; Silicate liquid immiscibility; Core-mantle boundary

* Corresponding author at: Museum für Naturkunde, Leibniz-Institut für Evolutions- und Biodiversitätsforschung, Invalidenstraße 43, D-10115 Berlin, Germany.
E-mail address: christopher.hamann@mfn-berlin.de (C. Hamann).

http://dx.doi.org/10.1016/j.gca.2016.10.042
0016-7037/© 2016 Elsevier Ltd. All rights reserved.

1. INTRODUCTION

Two varieties of iron meteorites can be distinguished: (i) the fractionally crystallized magmatic iron meteorites (IC, IIAB, IIC, IID, IIIAB, IIIE, IIIF, IVA, and IVB) and (ii) the silicate-bearing, so-called non-magmatic iron meteorites (IAB/IIICD and IIE), with several members containing silicate inclusions of various nature (Choi et al., 1995; Goldstein et al., 2009). While fractional crystallization of slowly cooling metallic liquids (Scott, 1972) is the process that formed the first variety, the exact formation conditions of the silicate-bearing irons are less clear. Their formation is inconsistent with extensive fractional crystallization and these irons may have come from bodies that were not sufficiently heated to form metallic cores (Haack and McCoy, 2004).

The iron meteorites belonging to the IIE group possess silicate inclusions representing a wide variety of characteristics, ranging from large chondritic clasts to smaller, molten, feldspar-rich globules (Ruzicka, 2014). Mittlefehldt et al. (1998) classified these different types into five groups while Ruzicka (2014), on the other hand, prefers to divide the silicate-bearing IIE into a fractionated and an unfractionated subgroup. Given the observation of a silicate inclusion made of impact melt lithology in Netschaëvo (Van Roosbroek et al., 2016), it is possible that IIE are impact melt breccias. This illustrates that there is no appropriate way to classify the very broad range of mineralogical and petrological characteristics the IIE represent.

Looking at their radioisotopic ages, the silicate-bearing IIE form two groups that do not correspond to the fractionated and unfractionated subgroups based on mineralogy. An "old" IIE group, having a formation age of ~4.5 Ga, consists of 6 meteorites: Weekeroo Station, Colomera, Miles, Techado, Taramuhara, and the recently described Mont Dieu, whereas meteorites sharing ages of around 3.6 Ga are called the "young" IIE; this group consists of Netschaëvo, Kodaikanal, and Watson (Bogard et al., 2000).

Over the past decades, several formation scenarios were proposed for the IIE group, trying to incorporate all their different features. These can be subdivided into *exogenic*, *endogenic*, and *hybrid models*. In exogenic models, IIE are formed by impact mixing with limited to complete impact melting (Burnett and Wasserburg, 1967; Bence and Burnett, 1969; Scott and Wasson, 1976; Osadchii et al., 1981; Rubin et al., 1986; Wasson and Wang, 1986; Olsen et al., 1994; Ikeda and Prinz, 1996; Ikeda et al., 1997). In endogenic models, IIE are formed as an internal process inside an early planetesimal, involving internal radiogenic heating followed by incomplete separation of metal and troilite from silicate (Wasserburg et al., 1968; Prinz et al., 1982, 1983; McCoy, 1995). Hybrid models consist of a combination of both extremes (Bunch et al., 1970; Armstrong et al., 1990; Casanova et al., 1995; Ruzicka et al., 1999; Bogard et al., 2000; Hsu, 2003; Takeda et al., 2003; Ruzicka and Hutson, 2010). Ruzicka (2014) subdivided them into three groups: (i) "cold crust models" where metallic melt is mixed with cold silicate at the surface of an asteroid as a consequence of an impact event, (ii) "hot mixing models" where metallic melt is injected, also as a consequence of an impact event, in an internally heated chondritic body, and (iii) "collisional disruption and re-accretion" models where the internally heated parent body broke up and re-accreted afterwards. All these formation models involve a chondritic parent body, the main H chondrite or a related H chondrite-like parent body.

Netschaëvo is the first iron meteorite where the occurrence of chondrules has been discovered and has long been regarded as the most primitive member of the IIE group. However, Van Roosbroek et al. (2016) described silicate inclusions not corresponding to the chondrule-bearing clasts, which can be classified as impact melt rocks. This suggests that Netschaëvo is a breccia containing metamorphosed and impact melt rock clasts (Van Roosbroek et al., 2016) and, consequently, that collisions must have played an important role in its formation history.

Following up on the initial petrographic description of the Netschaëvo impact melt rock inclusions by Van Roosbroek et al. (2016), the present study sets out a detailed nano-analytical investigation of the glassy material in the silicate inclusions of Netschaëvo IIE by means of electron microprobe analysis and transmission electron microscopy in order to gain more detailed insight into their formation mechanism. We show that the occurrence of phosphoran olivine (containing several wt% P_2O_5; *cf.* Boesenberg and Hewins, 2010) and the presence of silicate emulsion textures strengthen the impact formation hypothesis. We also constrain the temperature at which transfer of phosphorus from the metal into the silicate melt occurs—a process which may be important for core–mantle boundaries or other silicate–metal interaction zones, *e.g.*, in the source of pallasite meteorites (*cf.* McKibbin et al., 2016).

2. ANALYTICAL TECHNIQUES

2.1. Electron microprobe analysis

Back-scattered electron (BSE) imaging and quantitative electron microprobe analysis (EMPA) of the fine-grained, siliceous material in Netschaëvo were done with the JEOL JXA-8500F field-emission electron microprobe at Museum für Naturkunde, Berlin, Germany, which is equipped with five wavelength-dispersive X-ray spectrometers and an energy-dispersive X-ray spectrometer. Operating conditions for wavelength-dispersive X-ray spectrometry (WDX) were set to an acceleration voltage of 15 kV, a beam current of 15 nA, and a working distance of ~11 mm. A slightly defocused beam (spot size ~5 μm) was used for measuring the bulk composition of the fine-grained, siliceous material. Standardization was based on the main Astimex and Smithsonian international standards suite of the micro-analytical facilities at Museum für Naturkunde; see Table A1 (Appendix A) for details. Raw data were then processed for matrix effects using a conventional ZAF routine in the JEOL series operating system. Normalization of WDX analyses to 100 wt% was not applied and results are reported in oxides. Detection limits varied between 48 ± 1 ppm for Cl and 210 ± 1 ppm for Mn; see Table A1 for average values. Accuracy of the WDX analyses is much better than 3% for major ele-

ments >5 wt% and in the range of 10–15% for minor elements <0.5 wt%. Precision is much better than 5% for major elements >5 wt% and in the range of several ten percent for minor elements <0.5 wt%.

2.2. Transmission electron microscopy

Sample preparation as well as transmission electron microscopy (TEM) were both carried out at the TEM laboratory of the Deutsches GeoForschungsZentrum, Potsdam, Germany. Preparation of electron-transparent samples was done with a FEI FIB200TEM focused ion beam (FIB) device (for a detailed description of the FIB preparation method, see Wirth, 2009). A TEM-ready foil with final dimensions of 15 × 10 × 0.1 μm was cut directly from the polished and carbon-coated section using a gallium ion beam under high-vacuum conditions. Then, it was placed on a carbon film on top of a copper grid. Further carbon-coating to prevent charging of the TEM sample was not applied (for a discussion on the need of TEM sample carbon-coating, see Wirth, 2009).

The FIB-cut TEM foil was then surveyed and analyzed with a FEI Tecnai G^2 F20 X-Twin transmission electron microscope. The microscope is equipped with an EDAX ultra-thin window EDX system, a Fishione high-angle annular dark-field (HAADF) detector, and a Gatan imaging filter. Operating conditions were set to an acceleration voltage of 200 kV, using normal imaging mode for bright-field (BF) and dark-field (DF) imaging and scanning transmission electron microscopy (STEM) mode for HAADF imaging and analytical electron microscopy (AEM). All HAADF images were acquired with a camera length of either 75 or 330 mm. In general, the brightness of such images follows a Z^2 dependency (*e.g.*, Wirth, 2009). Specifically, a short camera length (75 mm) allows to image Z contrast (by collecting only electrons that were scattered under high angles from inner shell electrons), whereas a long camera length (330 mm) allows to simultaneously image Z contrast and diffraction contrast (by collecting electrons that were scattered under low angles from outer shell electrons). Bright-field images were digitally recorded, only electron diffraction patterns were recorded on image plates. Compositional information on both crystalline and amorphous phases was obtained semi-quantitatively from EDX spectra. Each EDX spectrum was obtained within 60–120 s live time. Beam size in STEM mode was ~1 to 2 nm. However, to avoid specimen damage and mass loss (especially of Na), the electron beam was scanned across a preselected area during data acquisition. Depending on specific count rates, the dead time of the utilized EDX spectrometer was mostly between 5 and 10%. For quantification, the k_{ab} factors of the TIA software package were used and all data were normalized to 100 wt%. Total errors for AEM are ~4% for concentrations of 5–30 wt% and >50% for concentrations below a few percent by weight. Structural information on crystalline and amorphous phases was either directly obtained with selected area electron diffraction (SAED) patterns recorded on image plates (allowing high precision), or by calculating diffraction patterns with a fast Fourier transform (FFT) from high-resolution lattice fringe images of lattice fringes (allowing fast data acquisition). Interpretation of acquired diffraction patterns was done with the program Digital Micrograph by Gatan.

3. PETROGRAPHY

The silicate inclusions of the impact melt rocks of Netschaëvo (Fig. 1) are characterized by a porphyritic texture dominated by coarse-grained olivine and, to a lesser extent, by pyroxene crystals. They are embedded in a groundmass containing fine-grained, euhedral olivine crystals set in quenched melt that is partially crystallized with microlitic domains consisting of olivine. Several opaque phases are present in the Netschaëvo silicate inclusions, the majority consisting of kamacite and taenite, usually present as large, irregular grains (300–400 μm) with lesser amounts of troilite. Metal is also found as rounded metal blebs (5–20 μm) surrounded by metal dendrites (1–5 μm) with an interstitial P–S-rich phase. Such globules are contained in the glassy material and also between and within olivine and pyroxene crystals. The glassy matrix material in the inner part of the silicate inclusion has a quasi-basaltic composition and contains a relatively high SiO_2 content, whereas the matrix material closer to the contact with the surrounding metal has lower SiO_2 and is enriched in P_2O_5, CaO, and FeO. The latter will be referred to as "silico-phosphate material" (Table 1). In the area containing the silico-phosphate material, euhedral Mg-chromite crystals of 10–100 μm and small (<2 μm), Si-rich globules are present. Olivine and pyroxene crystals have the same composition throughout the silicate inclusion, independent of the type of matrix material present. A detailed description of these samples is provided by Van Roosbroek et al. (2016).

4. MINERALOGY OF FINE-GRAINED MATERIAL

As some microstructural features are smaller than the resolution limit of the microprobe, TEM is required in order to characterize the fine-grained material in the inclusion. Thus, a TEM foil (Fig. 2a) was FIB-cut from a representative area of the silico-phosphate matrix material present at the outer rim of the silicate inclusion (*cf.* Fig. 1b).

4.1. Phosphoran olivine

Olivine is the most abundant phase in the fine-grained material. The olivine crystallites generally have elongated shapes and their sizes range from <500 nm to ~2 μm length and ~100 nm to ~400 nm width. They occur in a geometric, symplectitic network with interstitial glass (see Section 4.3) between individual olivine laths (Figs. 2b and 3a). Selected-area electron diffraction patterns (Fig. 4a) and HRTEM lattice fringe images (Fig. 5) indicate that olivine grains are perfectly crystalline, showing little or no signs of lattice defects or twinning. A SAED pattern of a typical olivine lath (Fig. 4a) was obtained with a low-index zone axis orientation (*i.e.*, electron beam parallel to c axis) and could be unequivocally identified as olivine.

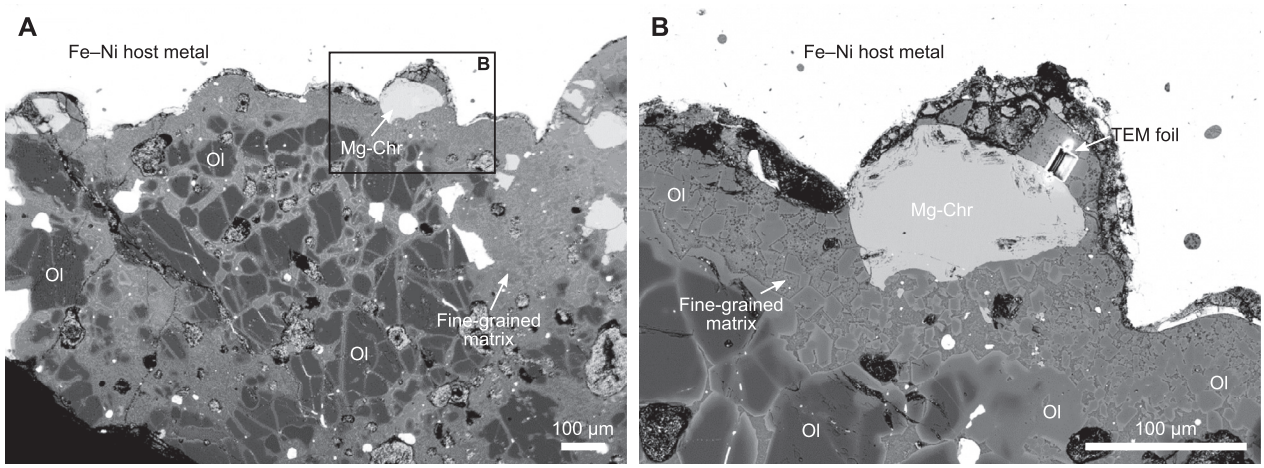

Fig. 1. Back-scattered electron images of the studied Netschaëvo silicate inclusion in contact with the host Fe–Ni metal. (a) Typical texture of the silicate inclusion, showing coarse-grained olivine (Ol) and Mg-chromite (Mg-Chr) crystals in fine-grained matrix. (b) Location of the TEM foil (Fig. 2a) representatively sampling the fine-grained matrix in contact with the Fe–Ni host metal. Note the presence of silicate droplets in the Fe–Ni host metal.

Table 1
Average composition and standard deviation of the glassy matrix material in Netschaëvo determined by electron microprobe analysis.

Quasi-basaltic material		Silico-phosphate material	
		SiO_2-poor	SiO_2–CaO-poor
SiO_2	53.4 ± 4.5	36.2 ± 3.0	40.7 ± 5.9
TiO_2	0.4 ± 0.1	0.3 ± 0.1	0.10 ± 0.05
Al_2O_3	7.6 ± 0.9	4.5 ± 1.1	3.3 ± 1.9
Cr_2O_3	0.2 ± 0.1	0.7 ± 0.3	0.5 ± 0.2
FeO	16.9 ± 2.9	21.9 ± 1.9	26.0 ± 1.9
MnO	0.3 ± 0.1	0.3 ± 0.1	0.30 ± 0.04
MgO	3.9 ± 1.3	7.2 ± 2.8	18.3 ± 7.8
CaO	10.6 ± 2.6	14.2 ± 3.0	1.7 ± 1.6
Na_2O	2.1 ± 0.6	1.1 ± 0.3	0.5 ± 0.5
K_2O	0.3 ± 0.2	0.2 ± 0.1	0.1 ± 0.1
P_2O_5	3.0 ± 2.0	12.1 ± 2.2	8.0 ± 0.7
NiO	bdl	0.04	0.04 ± 0.02
Cl	1.3 ± 0.3	1.9 ± 0.4	0.2 ± 0.2
Total	100.0	100.6	99.7
No. of analyses	10	12	4

Data were obtained by EMPA-WDX and are given in wt%; bdl = below detection limit.

Specifically, lattice spacing between the (100), (010), and (110) planes is ~4.65 Å, ~10 Å, and ~4.17 Å, respectively. Moreover, the angles between the (110) and (100) and the (110) and (010) planes are 24.7° and ~65°, respectively. Thus, the obtained SAED pattern agrees well with the olivine structure.

TEM-EDX analyses (Table 2) show that olivine contains up to 14 wt% of P_2O_5 and that olivine has an intermediate fayalite (Fa) content ranging from Fa_{42}–Fa_{47} on the left side of the TEM foil (where Cl-bearing apatite is absent) to Fa_{64} on the right side of the TEM foil (where it is in assemblage with Cl-bearing apatite and Fe sulfides). As apparent from the number of cations on the basis of four oxygen atoms (Table 2), Si deficiency is approximately counterbalanced by the presence of P, suggesting that Si + P ≈ 1 and that phosphorus replaces silicon in the olivine structure. This is best illustrated by olivine analysis Ol.2 (Table 2), which has an unusually low SiO_2 content of 21.4 wt% (equaling 0.72 Si atoms per formula unit) paired with the highest P_2O_5 content of 14.0 wt% (equaling 0.40 P atoms per formula unit). Although TEM-EDX analyses are less precise (and notoriously lack the high accuracy and precision of microprobe data), with Si + P ≈ 1 and the sum of the remaining cations close to 2, it seems likely that phosphorus is substituting for silicon in the olivine structure.

4.2. Cl-apatite

Cl-apatite occurs as interstitial dendritic chains consisting of intergrown apatite crystallites showing typical hopper morphologies and dimensions of ~250 nm (Figs. 2d, 3b, and 6). The chains are usually between 500 nm and 1 µm long, a single chain reaching a length of ~4 µm. Individual crystallites often show hollow cavities and are delicately intergrown with olivine crystallites, Fe-sulfide blebs, and interstitial glass (Fig. 6). A SAED pattern (Fig. 4b) was indexed as apatite; lattice spacing in $[11\bar{2}1]$, $[1\bar{1}00]$, and $[20\bar{2}1]$ direction is 3.86 Å, 8.19 Å, and 3.51 Å, respectively, and the angles between the $[11\bar{2}1]$ and $[20\bar{2}1]$ and the $[1\bar{1}00]$ and $[20\bar{2}1]$ directions are 25.3° and 64.4°, respectively. Additionally, TEM-EDX analyses show that Cl-apatite contains up to 4.5 wt% Cl (Table 2).

4.3. Amorphous material

A third phase in the residual material is not only present in the form of amorphous globules of about 500 nm to 1.5 µm diameter, but also as an amorphous groundmass interstitial to phosphoran olivine and Cl-apatite crystallites (Figs. 2 and 3). In the globules, amorphous secondary droplets of 10–50 nm diameter are finely dispersed (Figs. 2c, d,

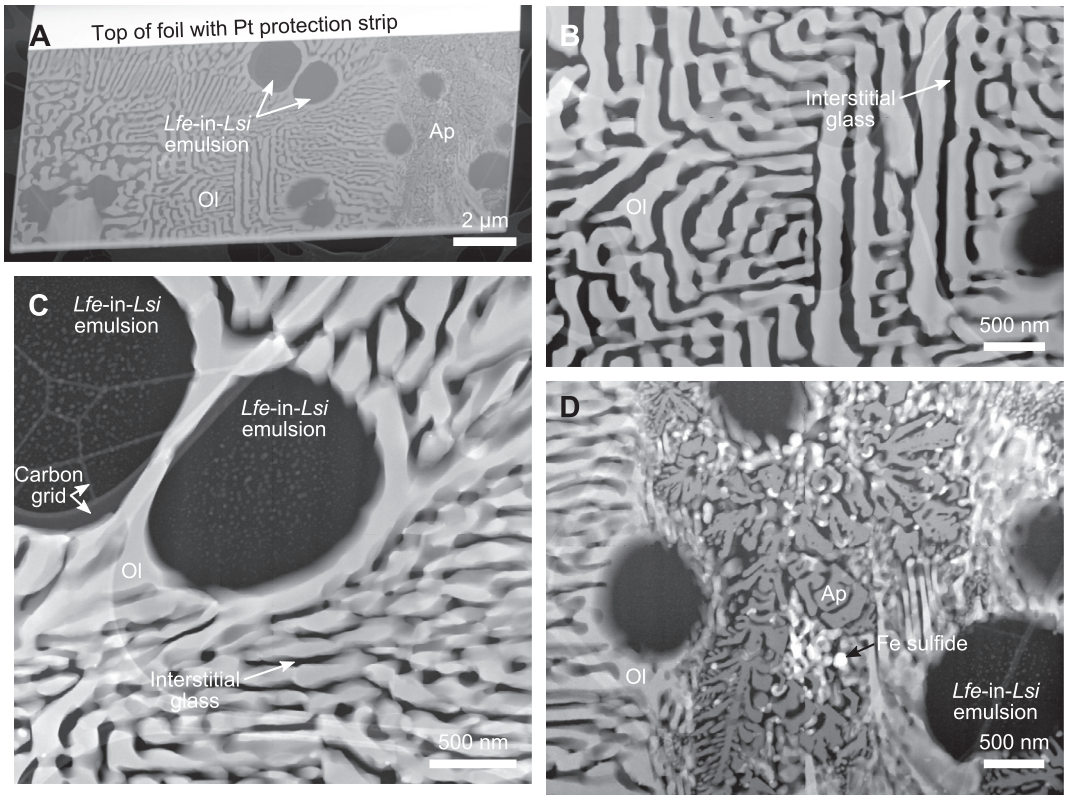

Fig. 2. High-angle annular dark-field TEM images showing the entire foil (a) and typical details (b–d). Phosphoran olivine (Ol) crystallites, grown in symplectite-like fashion (b), enclose globules of Si-rich glass and Cl-apatite (Ap) hopper crystals (c and d). Note that tiny droplets some 10–50 nm in diameter are disseminated in the globules (c), hinting at further (metastable?) liquid–liquid phase separation. The TEM carbon grid is weakly visible seemingly in front of the images. The first-order (stable) liquid immiscibility is indicated by *Lfe* (Fe-rich liquid) and *Lsi* (Si-rich liquid).

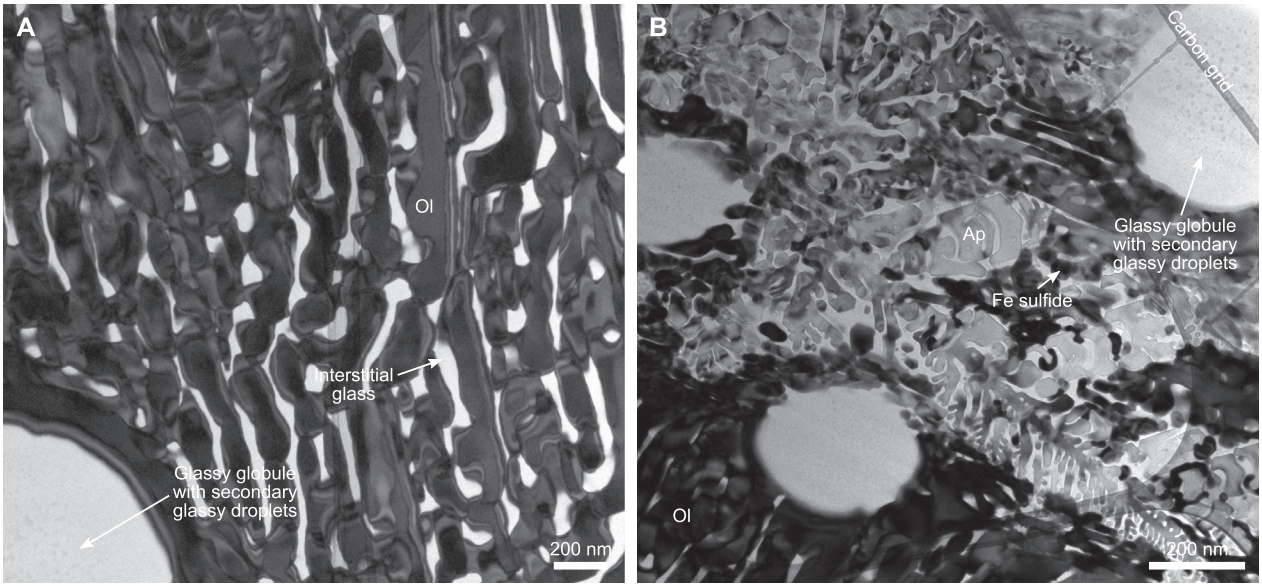

Fig. 3. Bright-field TEM images of phosphoran olivine, Cl-apatite, and glassy globules. (a) Symplectite-like texture of phosphoran olivine (Ol) crystallites and interstitial glass. The olivine crystallites show a common crystallographic orientation, as indicated by rather uniform diffraction conditions. Note that the glassy globule is surrounded by an olivine grain that grew around the globule. (b) Delicate intergrowth of phosphoran olivine, Cl-apatite (Ap) hopper crystals, glassy globules, and Fe sulfide blebs. Note the difference in diffraction contrast between crystalline (diffraction contrast visible) and amorphous phases (diffraction contrast absent).

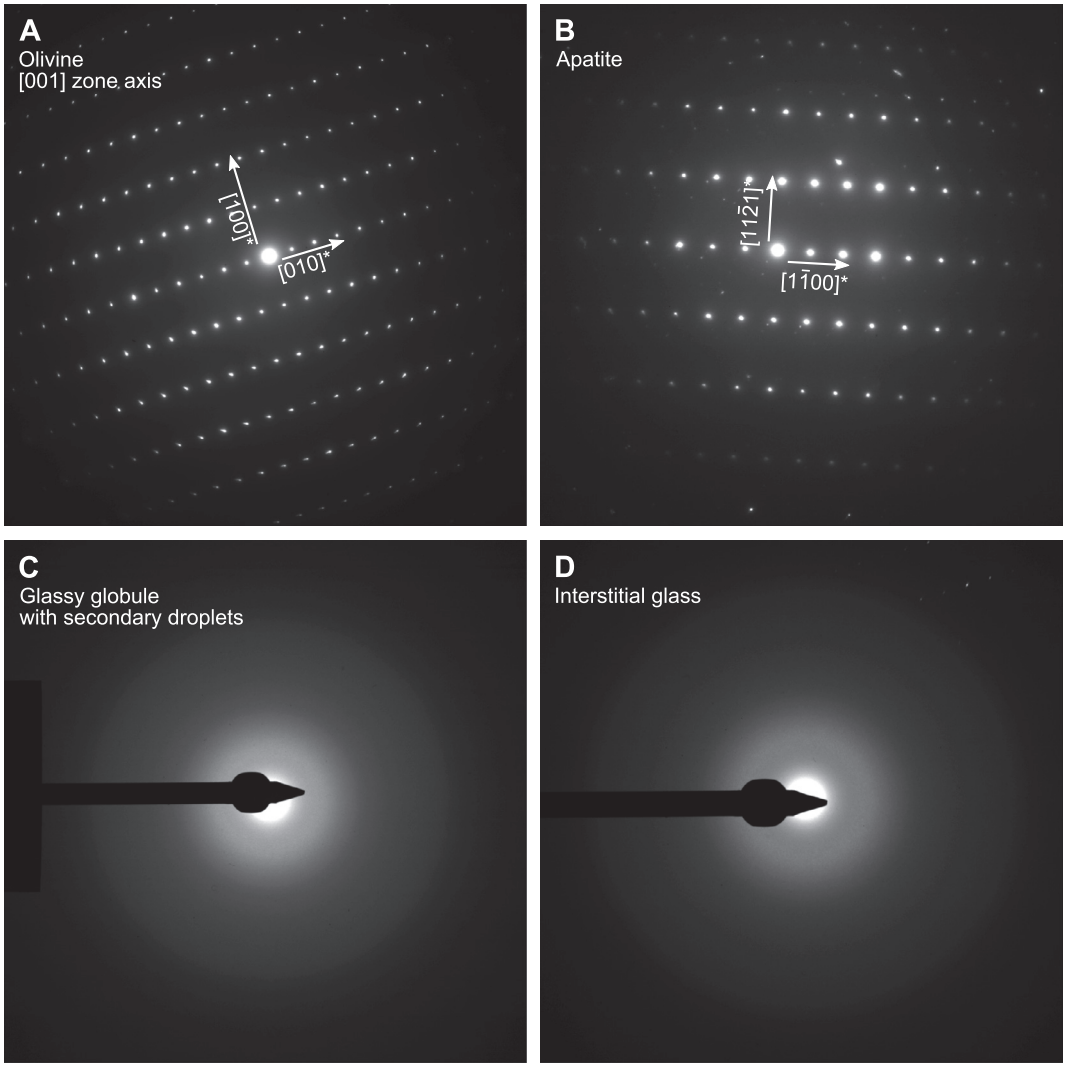

Fig. 4. Selected area electron diffraction patterns of crystalline (a and b) and amorphous (c and d) phases in the studied TEM foil. (a) Olivine diffraction pattern, obtained with an incident electron beam parallel to *c* axis. Lattice spacing between the (100), (010), and (110) planes is ~4.65 Å, ~10 Å, and ~4.17 Å, respectively. The angles between the (110) and (100) and the (110) and (010) planes are 24.7° and ~65°, respectively. (b) Apatite diffraction pattern; lattice spacing in [11$\bar{2}$1], [1$\bar{1}$00], and [20$\bar{2}$1] direction is 3.86 Å, 8.19 Å, and 3.51 Å, respectively. The angles between the [11$\bar{2}$1] and [20$\bar{2}$1] and the [1$\bar{1}$00] and [20$\bar{2}$1] directions are 25.3° and 64.4°, respectively. (e) Diffraction pattern of a glassy globule with secondary droplets (obtained from the large globule in the upper right corner of Fig. 3b), showing a set of diffuse, concentric rings that prove that the material is truly amorphous. (d) Diffraction pattern of the glass interstitial to olivine crystallites, also yielding a set of diffuse, concentric rings.

and 3a, b). Both materials—the globules with secondary droplets, as well as the groundmass interstitial to the crystalline phases—lack the typical diffraction contrast of crystalline materials in BF images (Fig. 3). Furthermore, SAED patterns (Fig. 4c, d) show sets of diffuse, concentric scattering intensity, ultimately confirming that both materials are completely amorphous.

In HAADF images (Fig. 2c), the globules show dark contrast, whereas the nanometer-sized droplets show bright contrast. Hence, the host material is composed of low-*Z* material, whereas the secondary droplets are composed of high-*Z* material (*Z* denotes atomic number). Specifically, the globules usually show a bulk composition rich in SiO_2 (75.0–86.5 wt%) with lesser amounts of Al_2O_3 (9.3–12.2 wt%) and FeO (2.8–4.1 wt%; see Table 3). Moreover, considerable compositional heterogeneity from globule to globule exists for Na_2O (below detection limit to 5.5 wt%), K_2O (<0.2–1.2 wt%) and CaO (0.9–2.1 wt%), which is often associated with the presence or absence of the small, nanometer-sized, high-*Z* contrast droplets. Due to the small dimensions of these droplets, reliable TEM-EDX analyses were not possible on individual droplets, as focusing the electron beam for EDX analyses immediately resulted in sputtering material from the TEM foil. The glass interstitial to phosphoran olivine and Cl-apatite is dominated by SiO_2 (79.1–89.2 wt%), with Al_2O_3 (8.9–11.3 wt%) and FeO (1.0–6.9 wt%) being present as minor components. Thus, it is compositionally similar to the glassy globules.

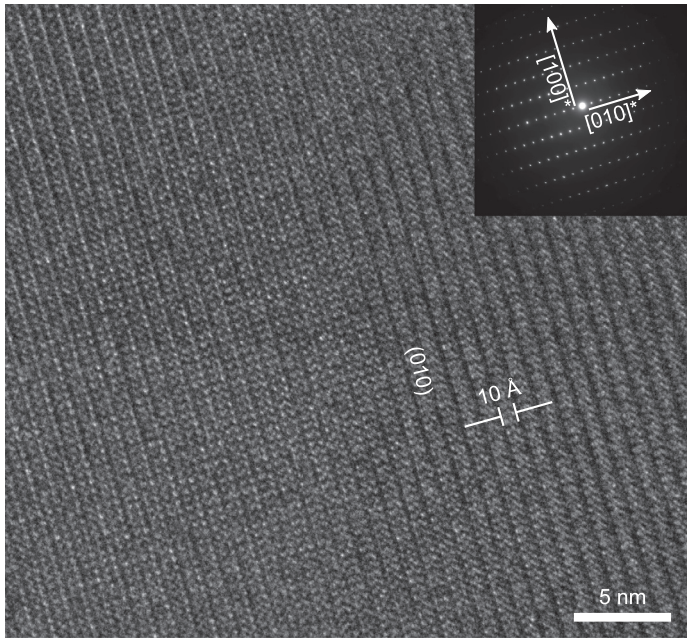

Fig. 5. High-resolution TEM image picturing lattice planes in a typical phosphoran olivine crystallite with a zone axis of [0 0 1]. The olivine crystal lattice is free of lattice defects or twinning, and lattice spacing of the (0 1 0) plane is ~10 Å. The inset shows the corresponding SAED pattern; see Fig. 4a for details.

Table 2
Composition of phosphoran olivine and Cl-apatite crystallites in the fine-grained matrix of the silicate inclusions in Netschaëvo determined by analytical transmission electron microscopy.

	Ol.1	Ol.2	Ol.3	Ol.4	Ol.5	Ap.1	Ap.2
	Olivine					Apatite	
Oxide wt%							
SiO_2	30.8	21.4	33.1	31.5	31.9	3.8	6.4
Al_2O_3	0.6	0.5	bdl	bdl	bdl	bdl	0.6
Cr_2O_3	bdl	bdl	bdl	bdl	bdl	bdl	bdl
FeO*	32.3	38.4	38.8	34.5	46.4	2.5	2.0
MnO	bdl	1.4	0.5	0.3	0.4	bdl	bdl
MgO	24.4	24.3	27.6	25.5	14.8	1.1	bdl
CaO	bdl	bdl	bdl	bdl	0.2	48.1	50.8
P_2O_5	11.8	14.0	bdl	7.1	6.3	40.2	35.8
Cl	bdl	bdl	bdl	bdl	bdl	4.3	4.5
Number of cations on the basis of four O							
Si	0.94	0.72	0.94	0.94	1.00	0.30	0.51
Al	0.02	0.02	–	–	–	–	0.06
Cr	–	–	–	0.02	–	–	–
Fe	0.82	1.08	0.93	0.86	1.21	0.16	0.13
Mn	–	0.04	0.01	0.01	0.01	–	–
Mg	1.11	1.22	1.17	1.13	0.69	0.13	–
Ca	–	–	–	–	0.01	4.08	4.37
P	0.30	0.40	–	0.18	0.17	2.69	2.43
Cl	–	–	–	–	–	0.58	0.61
Total	3.19	3.48	3.05	3.14	3.09	7.95	8.12
Fa†	42	47	44	43	64	–	–

Data were obtained by TEM-EDX and are fixed to 100 wt%; bdl = below detection limit.
* All Fe reported as FeO.
† Fa = 100 × Fe/(Fe + Mg + Mn).

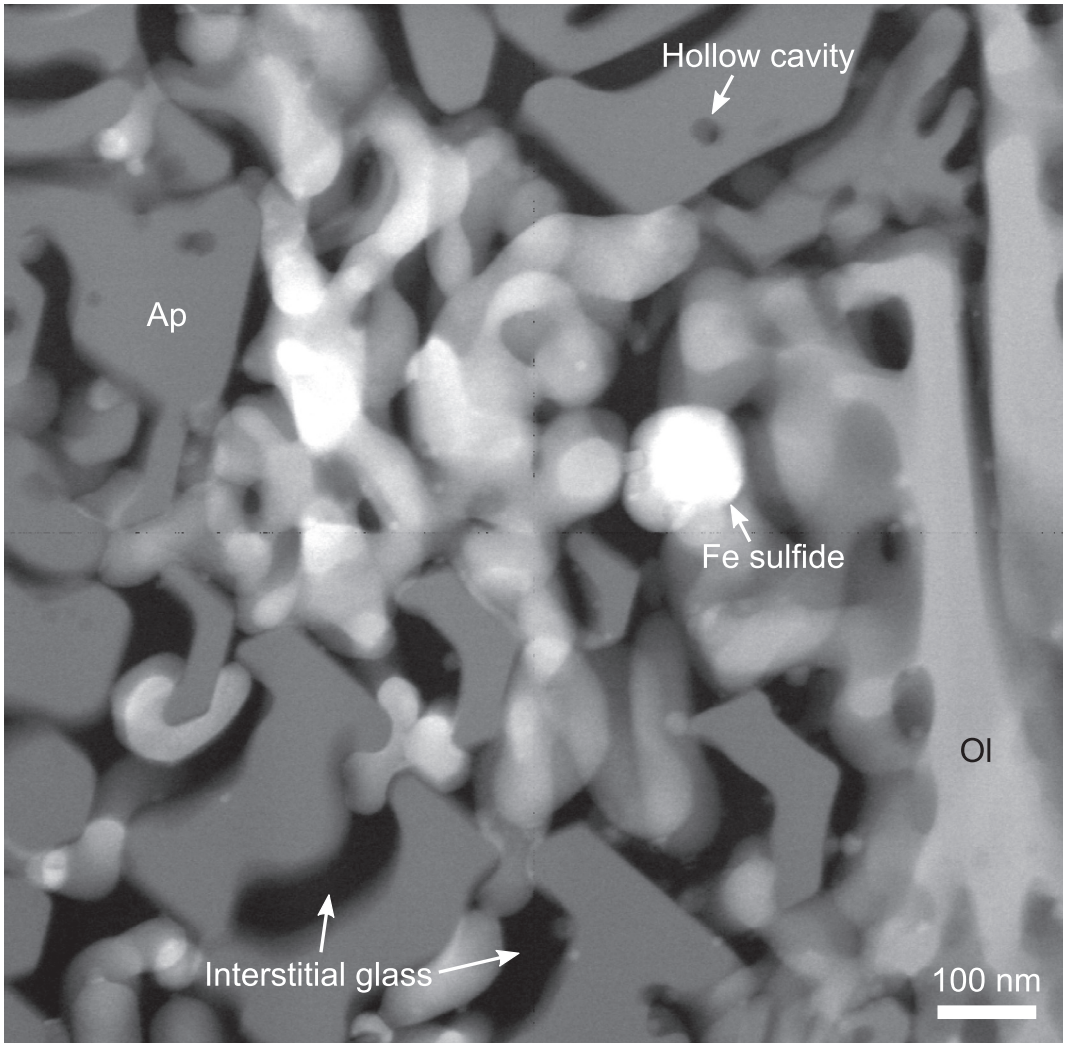

Fig. 6. High-angle annular dark-field TEM image showing the delicate intergrowth of Cl-apatite (Ap), phosphoran olivine (Ol), Fe-sulfides, and interstitial glass in detail (*cf.* Fig. 2d for an overview). Note the presence of hollow cavities in the Cl-apatite hopper crystals.

Table 3
Composition of interstitial glass and Si-rich, amorphous droplets (*Lsi*) in the fine-grained matrix of the silicate inclusions in Netschaëvo determined by analytical transmission electron microscopy.

	G.1	G.2	Average	σ	*Lsi*.1	*Lsi*.2	*Lsi*.3	*Lsi*.4	*Lsi*.5	Average	σ
	Interstitial glass, $n = 2$				Silica-rich, amorphous droplets (*Lsi*), $n = 5$						
SiO_2	89.2	79.1	84.2	2.3	75.0	86.5	85.0	85.0	80.9	82.5	1.9
TiO_2	bdl	0.6	<0.6	–	bdl	bdl	bdl	bdl	bdl	bdl	–
Al_2O_3	8.9	11.3	10.1	0.5	10.8	9.3	10.2	10.2	12.2	10.5	0.4
Cr_2O_3	bdl	bdl	bdl	–	bdl	bdl	bdl	bdl	bdl	bdl	–
FeO*	1.0	6.9	3.9	1.3	4.1	3.2	2.8	2.8	3.6	3.3	0.2
MnO	bdl	bdl	bdl	–	bdl	bdl	bdl	bdl	bdl	bdl	–
MgO	0.4	1.5	1.0	0.3	1.7	0.5	0.6	0.7	0.9	0.9	0.2
CaO	0.5	0.5	0.5	0.0	2.1	bdl	0.9	0.9	1.0	1.0	0.3
Na_2O	bdl	bdl	bdl	–	5.5	bdl	bdl	bdl	bdl	<5.5	–
K_2O	bdl	bdl	bdl	–	bdl	0.4	0.2	0.3	1.2	0.4	0.2
P_2O_5	bdl	bdl	bdl	–	bdl	bdl	bdl	bdl	bdl	bdl	–
Cl	bdl	bdl	bdl	–	0.8	0.1	0.2	bdl	0.1	0.3	0.1

Data were obtained by TEM-EDX and are fixed to 100 wt%; σ = standard error; bdl = below detection limit.
* All Fe reported as FeO.

The glassy globules are usually surrounded by phosphoran olivine crystallites, which, in some cases, seemingly grew around the glassy globules (Fig. 2c). The interface between host silicate glass and secondary glass droplets is, even under highest magnification, always a sharp meniscus rather than a gradual transition of composition. Furthermore, the secondary droplets cluster in the cores of their host globules, leaving a narrow zone almost free of secondary droplets adjacent to the interface with the surrounding olivine (Fig. 2c).

4.4. Metallic globules

Metallic globules of 100 nm to 60 μm diameter are disseminated in the silicate inclusion. Usually, these globules consist of an intergrowth of two or three phases (Fe-rich, S-rich, and possibly with an additional P-rich phase). Microprobe measurements indicate that the Fe-rich phase in the globules comprising the three phases consist of a Ni-poor phase (87.3 wt% Fe and 10.1 wt% Ni) and a Ni-rich phase (66.9 wt% Fe and 32.4 wt% Ni). The S-rich phase consists of 62.6 wt% Fe and 33.8 wt% S, whereas the P-rich phase consists of 60.7 wt% Fe, 24.5 wt% Ni, and 13.8 wt% P.

5. DISCUSSION

5.1. Phosphoran olivine

Phosphoran olivine is an extremely rare phase, being described for the first time in pallasites (Buseck, 1977; Buseck and Clark, 1984). It is generally referred to as "phosphoran" if more than 1 wt% P_2O_5 is present (Boesenberg and Hewins, 2010). For example, Wasson et al. (1999) found up to 7.4 wt% P_2O_5 in phosphoran olivine from the Brenham pallasite. This mineral has also been found in terrestrial (Goodrich, 1984; Agrell et al., 1998) and other extraterrestrial samples (Buseck and Clark, 1984; Wasson et al., 1999; Goodrich, 2003; Wang et al., 2006), as well as in manufactured objects (Tropper et al., 2004; Boesenberg, 2006). In olivine, P^{5+} will replace Si^{4+} in the silica tetrahedron, but requires charge balancing with another cation. Early studies suggested that P^{5+} and Na^{+} substitute for Si^{4+} and Mg^{2+} (or Ca^{2+}), as is the case for garnets (Thompson, 1975; Bishop et al., 1976). However, Na^{+} cannot be accommodated by olivine, as there is no structural site available for this cation (Goodrich, 1984). Buseck and Clark (1984) were the first to propose the possibility of vacant octahedral sites that compensate for the charge of P^{5+}. Goodrich (1984) supported this idea, based on structural formula of olivine showing cation deficiencies. The vacancy of the octahedral site was experimentally confirmed by Boesenberg and Hewins (2010), who proposed the charge balancing scheme $4^{VI}M^{2+} + 2^{IV}Si^{4+} \leftrightarrow 3^{VI}M^{2+} + 2^{IV}P^{5+} + {}^{VI}[]$.

Boesenberg and Hewins (2010) carried out experiments to constrain the formation conditions of phosphoran olivine and concluded that three requirements need to be met: (i) enrichment of P_2O_5 in the parental melt, (ii) depletion of SiO_2 in the parental melt, and (iii) rapid crystallization from a melt or rapid cooling in an un-equilibrated system. The latter is inferred from their findings that P behaves compatibly within the first tens of hours of the experiments ($D^{Ol/Liq} > 1$), resulting in the incorporation of P into the olivine, but becomes highly incompatible ($D^{Ol/Liq}$ is 0.001–0.3) after a timescale of days to weeks, and will be expelled from the crystal lattice and be replaced by Si. Based on their experiments, Boesenberg and Hewins (2010) concluded that phosphoran olivine crystallized from a melt supersaturated in P, by igneous activity or a pyrometamorphic reaction.

5.2. Crystal shape and crystallization of Cl-apatite

The skeletal and parallel arrangements of apatite crystals in the Netschaëvo silicate inclusions can be produced by quenching from a liquid (Wyllie et al., 1962), while near-equilibrium growth produces smaller, equant apatites co-existing with liquid or vapor. Quench apatites produced experimentally (Wyllie et al., 1962) are generally closely-packed bundles of parallel or radiating needle aggregates. These bundles exhibit a hexagonal outline with interstitial, quenched glass in cross-section. Acicular crystals are greatly elongated parallel to the *c*-axis and can locally contain a hollow cavity along the length of the crystal. Wyllie et al. (1962) concluded that these crystal habits are present in experimental and natural systems over a wide range of compositions, indicating that the physical control of precipitation from a cooling liquid is the main driving force to form these crystals, while its chemical environment seems less important. Furthermore, acicular apatite crystals have been found in several environments (Girault, 1966; Capdevilla, 1967; Bargossi et al., 1999) and their presence has often been used to infer rapid cooling conditions and/or the presence of a fluid (Piccoli and Candela, 2002).

Several studies have investigated the solubility of apatite in melts. Although most studies have focused on felsic systems, Watson (1979) reported that saturation of apatite in basic to intermediate magmas is controlled by three variables, *i.e.*, concentration of P_2O_5, concentration of SiO_2, and temperature. The experiments were carried out over a temperature range of 1165–1275 °C and at 1 atm pressure. In a magma containing about 45 wt% SiO_2, ~6 wt% P_2O_5 is required for apatite saturation at 1200 °C. With increasing amounts of SiO_2 and with decreasing temperature, the amount of P_2O_5 needed to saturate the melt decreases. This indicates that high P_2O_5 concentrations are needed to saturate basaltic liquids. Furthermore, the amount of CaO has also an effect on apatite saturation (Tollari et al., 2006). In contrast to SiO_2, which is negatively correlated to the apatite saturation temperature, CaO encourages apatite saturation (Tollari et al., 2008). Furthermore, all experiments performed on ferrobasaltic liquids (Watson, 1980; Tollari et al., 2006, 2008) showed that pressure only has a minor effect on apatite saturation.

5.3. Silicate liquid immiscibility

From the observations made above—Si-rich silicate glass globules showing a secondary population of (presum-

ably Fe-rich) silicate glass droplets—it has to be considered that silicate liquid immiscibility affected the crystallization history of the fine-grained silicate matrix during cooling. In fact, liquid–liquid phase separation through immiscibility is a common phenomenon in glass-forming binary and multicomponent silicate systems. For example, it is frequently encountered and utilized in the production of technological glasses (*e.g.*, Shelby, 2005). On the contrary, in geosciences, the relevance of silicate liquid immiscibility has been debated since the early 20th century (*e.g.*, Daly, 1914; Bowen, 1928; Roedder, 1979; Philpotts, 1982; Veksler et al., 2007; Charlier et al., 2013, and references therein), and thus far, it seems that no consensus has been reached regarding its petrogenetic role and importance. However, despite its controversial reputation in geologic and planetary sciences, a large number of case studies on silicate emulsions exist in the literature. These have addressed terrestrial (*e.g.*, Philpotts, 1982) and lunar (*e.g.*, Roedder and Weiblen, 1970, 1971) basalts, terrestrial layered intrusions (*e.g.*, Jakobsen et al., 2005), natural (*e.g.*, Zolensky and Koeberl, 1991; Hamann et al., 2013) and experimental (Ebert et al., 2013) impact melts, and meteorites (e.g., Ruzicka et al., 2006).

The physical mechanism behind the unmixing process is quite universal and based on thermodynamics and the behavior of a system's Gibbs free energy of mixing, ΔG_m. Briefly, if mixing of two components yields a lower ΔG_m, the mixture will remain homogeneous, whereas if separation of the mixture into two components yields a lower ΔG_m, the mixture will (if allowed by kinetics) separate into two phases (James, 1975; Wood and Hess, 1980; Shelby, 2005). Phase separation in glass-forming silicate systems is in addition a consequence of the poor steric compatibility between network-forming (mainly Si^{4+}) and network-modifying (*e.g.*, Fe^{2+}, Mg^{2+}, and Ca^{2+}) cations and, furthermore, the Coulomb repulsion between poorly shielded network-modifying cations (Hudon and Baker, 2002). In a silicate melt, network-modifying cations are surrounded by bridging (Si–O–Si) and non-bridging (Si–O–M, where M is a network-modifying cation) oxygens that isolate the network-modifying cations from each other by masking the positive charges (Charlier et al., 2015). However, the bridging oxygens are connected to Si^{4+} by strong covalent bonds and, therefore, the network-modifiers are not well protected from each other, resulting in Coulomb repulsions and eventually in melt unmixing (Hudon and Baker, 2002). Typical textures of immiscibility comprise spherical globules or droplets of one phase disseminated in a continuous matrix phase. The interface between the two phases is always a sharp meniscus, which proves to be a good test for true immiscibility (*e.g.*, Roedder, 1978), since incomplete mixing of two (or more) melts with differing compositions will produce compositional gradients. Geologically relevant compositions tend to split up into a Si-rich liquid (*Lsi*) showing the composition of a granite, and an Fe-rich liquid (*Lfe*) showing the composition of an Fe-rich pyroxenite (Philpotts, 1982). Moreover, aluminum and alkalis tend to concentrate in *Lsi*, whereas the remaining major elements (especially Fe, Mg, Ca, and P) tend to concentrate in *Lfe*. After phase separation in the liquid state, rapid quenching is required in order to preserve the two phases, as crystallization (especially of the Fe-rich liquid, forming magnetite, Fe-rich olivine, or Fe-rich pyroxene) tends to destroy the evidence for liquid immiscibility (*e.g.*, Roedder, 1978; Philpotts, 2008).

The textures presented in Figs. 2 and 3 are unequivocally consistent with phase separation through silicate liquid immiscibility and they are the first clear occurrence of silicate liquid immiscibility in meteorites. They show globules of *Lsi* disseminated in an Fe–Mg–P-rich matrix, which crystallized to phosphoran olivine and Cl-apatite. Hence, the presence of one of the two phases (*i.e.*, *Lsi*) produced by liquid immiscibility is immediately apparent, whereas the conjugate matrix phase (*i.e.*, *Lfe*) crystallized during quenching to phosphoran olivine and Cl-apatite. However, the *mechanism* of phase separation is less clear. On one hand, the large glassy globules are consistent with phase separation through nucleation and growth of individual droplets (*cf.* James, 1975; Shelby, 2005). In this case, immiscible droplets nucleate randomly upon unmixing from the conjugate matrix phase, continuously growing by a process called Ostwald ripening. Phase separation by nucleation and growth is restricted to a region between the binodal and the spinodal of a miscibility gap (for a discussion of the binodal and the spinodal, see James, 1975; Shelby, 2005). Typical emulsion textures produced by nucleation and growth comprise spherical droplets of the dispersed phase randomly distributed in the matrix phase. On the other hand, the symplectitic texture formed by the phosphoran olivine and the interstitial *Lsi* is reminiscent of phase separation through spinodal decomposition (*cf.* James, 1975; Shelby, 2005), which ultimately results in an emulsion texture with high connectivity. Phase separation through spinodal decomposition will occur in that region of a miscibility gap that is defined by the spinodal. In that case, the dispersed phase will be regularly instead of randomly distributed in the matrix phase, forming tubes or continuous pathways. Hence, it is entirely possible that the silicate inclusions in this impact melt rock document both mechanisms of phase separation in a miscibility gap.

5.4. Formation of the silicate inclusion

The impact melt rocks of Netschaëvo were probably produced by shock melting and likely originated from the same parent material as the chondrule-bearing clasts, based on their similar composition (*cf.* Van Roosbroek et al., 2016). High temperatures must have been reached to melt a large part of the olivine. Large low-Ca pyroxene and olivine grains were preserved from melting, whereas small olivine and low-Ca pyroxene, together with calcic pyroxene, plagioclase, and phosphates, completely melted (*cf.* Van Roosbroek et al., 2016). At this stage the metal must also have been partially molten, as evidenced by the presence of quench features in the metal host and the scalloped contact between the silicate inclusion and surrounding metal (*cf.* Van Roosbroek et al., 2016). Upon cooling of the metal–silicate assemblage, several events took place that probably occurred in the following order: (i) precipitation of olivine and pyroxene from the liquid, (ii) phosphorus

in liquid metal–sulfide is oxidized and re-partitions into the silicate melt, (iii) silicate liquid immiscibility occurs, possibly due to high P_2O_5 contents, and (iv) phosphoran olivine and Cl-apatite crystallize during a late quenching event from *Lfe*, whereas *Lsi* quenched to a glass. In the following sub-sections, we place some quantitative constraints on these events.

5.4.1. Precipitation of olivine from the melt: estimation of temperature

Roeder and Emslie (1970) experimentally investigated olivine–liquid equilibria and presented a model to predict the temperature at which olivine will saturate in a liquid. This model is based on two important observations. The first is that the ratio

$$\frac{(X^{\mathrm{Ol}}_{\mathrm{FeO}})(X^{\mathrm{Liq}}_{\mathrm{MgO}})}{(X^{\mathrm{Liq}}_{\mathrm{FeO}})(X^{\mathrm{Ol}}_{\mathrm{MgO}})}$$

is nearly constant over a wide range of temperatures. The second observation is that the ratio

$$\frac{X^{\mathrm{Ol}}_{\mathrm{MgO}}}{X^{\mathrm{Liq}}_{\mathrm{MgO}}}$$

is highly temperature-dependent. Putirka (2005) recalibrated the model of Roeder and Emslie (1970), incorporating the effect of temperature, SiO_2, Na_2O, K_2O, and H_2O with the parameterizations:

$$\begin{aligned}\ln K_{\mathrm{D}}(\mathrm{Mg}) = &-2.106193(\pm 0.07) + 3063.2(\pm 87.4)/T(^{\circ}C)\\ &+ 0.019(\pm 0.001)[\mathrm{SiO_2}]^{\mathrm{Liq}}\\ &+ 0.080(\pm 0.002)[\mathrm{Na_2O} + \mathrm{K_2O}]^{\mathrm{Liq}}\end{aligned} \tag{1}$$

$$\begin{aligned}\ln K_{\mathrm{D}}(\mathrm{Fe}) = &-3.25(\pm 0.09) + 2556.4(\pm 114.6)/T(^{\circ}C)\\ &+ 0.028(\pm 0.002)[\mathrm{SiO_2}]^{\mathrm{Liq}}\\ &+ 0.052(\pm 0.003)[\mathrm{Na_2O} + \mathrm{K_2O}]^{\mathrm{Liq}}\end{aligned} \tag{2}$$

and obtained an olivine saturation surface that was temperature-sensitive and independent of olivine-composition. This model is used here to find the temperature at which fine-grained olivines precipitate from the Netschaëvo quasi-basaltic liquid. The average composition of the fine-grained olivines ($Fa_{24.5\pm3.8}$; Van Roosbroek et al., 2016) and the average composition of the quasi-basaltic melt is used (Table 1) to reconstruct a Netschaëvo parental melt as a mixture of the observed 80% quasi-basaltic groundmass and 20% olivine crystals (*i.e.*, in-situ crystallization of the quasi-basalt with an olivine component being removed from the melt). The quasi-basaltic melt is the most likely parental composition, because high phosphorus contents are only observed at the margins of the silicate inclusion, and phosphorus had not yet partitioned into the silicate melt by the time of fine-grained olivine precipitation (before separation of immiscible silicate melts). This is also based on the observation that there is no detectable P_2O_5 in the fine-grained olivine (*i.e.*, it is not phosphoran olivine) and on the likely temperature range at which these immiscible melts formed (see 5.4.3). Based on this model, a temperature of 1350–1400 °C best reproduces the composition of the Netschaëvo parental melt. The best matching composition, calculated by the model, was then used to calculate $X^{\mathrm{Ol}}_{\mathrm{MgO}}$ and $X^{\mathrm{Ol}}_{\mathrm{FeO}}$. The calculated composition of olivine is 35.5 wt% MgO and 21.1 wt% FeO, which corresponds well to the composition of the fine-grained olivines (37.9 ± 3.1 wt% MgO and 21.9 ± 2.9 wt% FeO; Van Roosbroek et al., 2016), indicating that the model is internally consistent. The calculated exchange coefficient K_{D}

$$K_{\mathrm{D}} = \frac{X^{\mathrm{Liq}}_{\mathrm{Mg}}/X^{\mathrm{Ol}}_{\mathrm{Mg}}}{X^{\mathrm{Liq}}_{\mathrm{Fe^{2+}}}/X^{\mathrm{Ol}}_{\mathrm{Fe^{2+}}}} \tag{3}$$

from the model, using these olivine compositions and the composition of the best-matching melt, is 0.32, in good agreement with typical K_{D} values of 0.31–0.34 for experiments on similar meteoritic melts (*e.g.*, experiments of Usui et al., 2015) and clearly in the general range of 0.17–0.45 for basaltic systems (*e.g.*, Putirka, 2005). These calculations further indicate that olivine precipitated in the Netschaëvo silicate inclusion in the relatively high temperature range of 1350–1400 °C.

5.4.2. Re-partitioning of phosphorus from the metal into the silicate phase

The silico-phosphate matrix material is concentrated in a 100-μm-wide rim at the edge of the silicate inclusion, close to the contact with the metal host. The area also contains small, SiO_2-rich globules spread in the fine-grained matrix and 10–100-μm-size Mg-chromite grains (Fig. 1). Based on the presence of Mg-chromite grains and the high amount of phosphorus in this region, resulting in the presence of phosphoran olivine and apatite, we can reasonably assume that phosphorus and chromium from the surrounding metal partitioned into the silicate melt. This is supported by (i) the low amounts of Cr_2O_3 and P_2O_5 in the chondrule-bearing Netschaëvo silicates, representing the original material (0.59 wt% and 0.54 wt% in the bulk silicate, respectively; Olsen and Jarosewich, 1971), (ii) the low concentration of P_2O_5 in the quasi-basaltic melt and the absence of chromite grains in the inner part of the silicate inclusion, and (iii) the presence of elongated intergrowths in the metal host of the investigated Netschaëvo silicate inclusion (Van Roosbroek et al., 2016), consisting of a P-rich, a S-rich, and an Fe–Ni phase. These intergrowths are connected to the edge of the silicate inclusion (Fig. 1b in Van Roosbroek et al., 2016), indicating that phosphorus was supplied to the silicate melt from the metal via these structures. A similar situation is present in olivine coronas on olivine grains in the Morristown and Emery mesosiderites. In these coronas, P and Cr are enriched and this can be explained by the diffusion of P and Cr from the metal (Ruzicka et al., 1994).

Several authors have investigated the metal–silicate partitioning of phosphorus (Newsom and Drake, 1983; Jana and Walker, 1997a,b; Pak and Fruehan, 1986; Young et al., 1992). The most recent study by Righter et al. (2010) experimentally investigated the effect of temperature and melt composition on $D_{\mathrm{P}}^{\mathrm{Met/Sil}}$ and observed that $D_{\mathrm{P}}^{\mathrm{Met/Sil}}$ increases with increasing temperature and decreases with

increasing polymerization of the melt. However, the findings of these studies are not easily applied quantitatively, because silicate and metal in Netschaëvo meet at a reaction zone, and clear zoning of olivine crystals in the silicate and the presence of discrete taenite crystals in the metal indicate a cooling and crystallization history. With cooling, the partitioning of phosphorus between metal and silicate changed, resulting locally in high P_2O_5 in silicate along reaction boundaries with the metal. This means that the composition of the silicate melt, and thus the polymerization degree, cannot be used to deduce a $D_P^{Met/Sil}$ value. Righter et al. (2010) showed that $D_P^{Met/Sil}$ depends mainly on the composition of the silicate material and much less on the temperature. Although no $D_P^{Met/Sil}$ value can be defined for Netschaëvo, the process is probably similar to the process responsible for the precipitation of oxide phases (*e.g.*, phosphates and chromites) in IIIAB iron meteorites (Olsen et al., 1999). During cooling and solidification of the metal, fractional crystallization takes place and taenite precipitates. Other elements are concentrated in the residual liquid, such as Na, Mg, K, Ca, Mn, P, Cr, (Olsen et al., 1999) and, importantly, O (Kracher, 1983). A large degree of taenite crystallization, or in another sense a low degree of partial melting, would yield a high concentration of O and P in the liquid metal. This concentration could also be explained by an unusual metal composition. The metal in Netschaëvo has a P concentration of 0.15 wt% (Buchwald, 1975), which can be compared to the P concentration in other IIE metal (0.15 wt%, 0.7 wt%, 0.3 wt%, 0.47 wt%, and 0.38 wt% for Weekeroo Station, Colomera, Kodaikanal, Elga, and Mont Dieu, respectively; Buchwald, 1975; Van Roosbroek et al., 2015). Therefore, the build-up of P and O can best be explained by fractional crystallization of the metal. With increasing oxygen fugacity, phosphorus can become oxidized. Initially, phosphorus preferentially resides in the molten metal, because $D_P^{Met/Sil}$ is high at high temperature (Schmitt et al., 1989; Chabot and Drake, 2000; Righter and Drake, 2000; Righter et al., 2010). However, during cooling, $D_P^{Met/Sil}$ decreases and phosphorus is expelled from the metal, partitioning into the silicate melt that is enclosed by the metallic liquid. The outer part of the silicate inclusion is enriched in P_2O_5, close to the contact with the metal host, while the inner part of the inclusion retains its quasi-basaltic composition. The presence of P_2O_5-rich rims on silicate inclusions and elongated intergrowths in the metal host consisting of a P-rich, a S-rich, and an Fe–Ni phase (Van Roosbroek et al., 2016) indicates that the system might approximate a phosphide–phosphate redox buffer, *i.e.*, part-way through the oxidation reaction (*cf.* Olsen et al., 1999).

The same probably also happened for Cr, enriching the melt in Cr_2O_3, which can explain the presence of Mg-chromite grains in the silicate inclusion along the contact with the surrounding metal (Fig. 1). It should be noted that chromite is a very early-crystallizing phase in IIIAB irons and pallasites, while phosphates are late-crystallizing phases. However, the situation may not be directly comparable with Netschaëvo because of the more complex silicate mineralogy (including pyroxene) and the presence of more major element components (*e.g.*, Al_2O_3 and TiO_2) likely influencing relative phase stabilities and, hence, crystallization order or timing. In terrestrial systems, chromite can crystallize directly from Fe–S–O mattes, and at chromite saturation there may be several tenths of a percent each of Cr and O in the melt (*e.g.*, Ulff-Møller, 1985, 1998; Fonseca et al., 2008). The in-situ generation of oxide, including phosphate, minerals from a low-degree melt of meteoritic iron therefore appears possible; nevertheless the introduction of an additional oxidizing agent cannot yet be entirely ruled out.

The effect of high phosphorus contents on silicate liquid structure has been investigated by several authors (Toplis et al., 1994; Bogaerts and Schmidt, 2006; Charlier and Grove, 2012). High P_2O_5 in a silicate melt will form PO_4^- complexes (Mysen and Richet, 2005) and, as a consequence, silicate polymerization increases, with a decrease in the number of non-bridging oxygens per tetrahedral cations (NBO/T). Higher polymerization results in a lower capacity to accommodate network-modifying cations (such as Ca^{2+}, Mg^{2+}, and Fe^{2+}). The PO_4^- complexes fit poorly into the silicate network and the free energy of the system increases, consequently expanding the liquid–liquid miscibility gap (Bogaerts and Schmidt, 2006). This, together with the fact that addition of phosphorus into the silicate liquid lowers the liquidus temperature (Toplis et al., 1994), promotes unmixing (Charlier and Grove, 2012). Phosphorus is, thus, enriched in the poorly polymerized melt *Lfe*, whereas silica is enriched in the polymerized melt *Lsi*. The same holds for other network-modifying cations, such as Ca^{2+}, Mg^{2+}, and Fe^{2+}.

5.4.3. Formation of immiscible melts

As outlined above, partitioning of phosphorus from the host metal into the silicate melt most likely induced liquid–liquid phase separation of *Lfe* and *Lsi*. Constraining a temperature at which unmixing was induced is, however, difficult, since laboratory experiments aiming at confining two-liquid fields (*e.g.*, Roedder, 1978; Bogaerts and Schmidt, 2006; Veksler et al., 2008, and references therein) for geologically relevant compositions are generally conducted under idealized equilibrium conditions. Attainment of chemical equilibrium is questionable for impact melts (*cf.* Hamann et al., 2016), mainly due to fast cooling rates and short durations at which materials stay in the liquid state. However, when plotted in the pseudo-ternary system ($CaO–MgO–FeO–TiO_2–P_2O_5$)–SiO_2–($Na_2O–K_2O–Al_2O_3$), *Lsi* and the interstitial glass between phosphoran olivine crystallites fall close to *Lsi* encountered in the mesostasis of terrestrial basalts (Fig. 7; *cf.* Philpotts, 1982). Moreover, the bulk composition of the quasi-basaltic melt (Table 1) falls right within the low-temperature two-liquid field, and tie lines connecting individual *Lsi* analyses with analyses obtained from phosphoran olivine—which is presumed to have crystallized from the conjugate melt, *Lfe*—are more or less parallel to the low-temperature two-liquid field (Fig. 7b). Furthermore, if we calculate a theoretical bulk composition of the assemblage phosphoran olivine + *Lsi* by means of calculating the volume fraction of both phases from HAADF images with the program ImageJ, we find

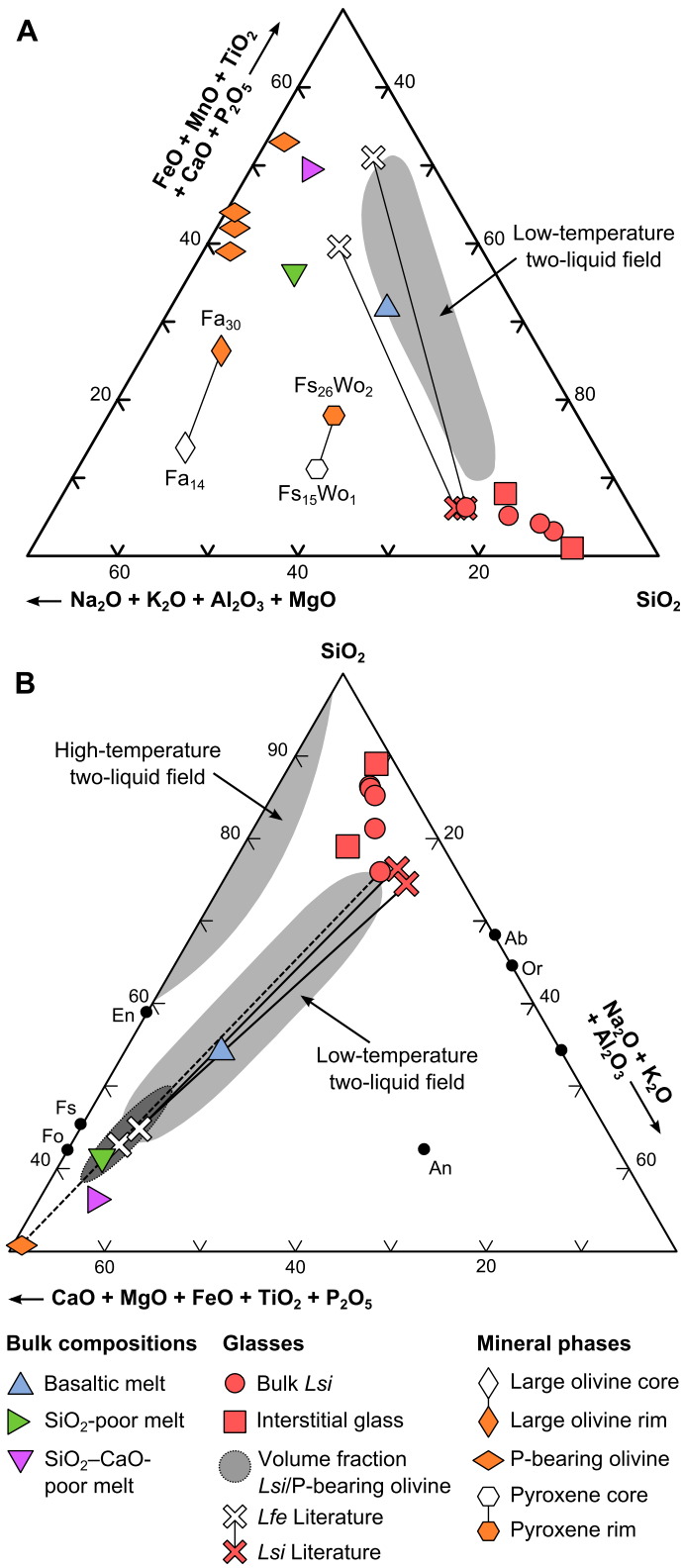

Fig. 7. Liquid immiscibility in the Netschaëvo silicate inclusion. (a) Pseudo-ternary system (Na_2O–K_2O–Al_2O_3–MgO)–(FeO–MnO–TiO_2–CaO–P_2O_5)–SiO_2 after Philpotts (1982). (b) Pseudo-ternary system (CaO–MgO–FeO–TiO_2–P_2O_5)–SiO_2–(Na_2O–K_2O–Al_2O_3) after Roedder (1978). Bulk melt composition is from Van Roosbroek et al. (2016), data of immiscible melts typically encountered in terrestrial volcanic rocks are from Philpotts (1982) and Sensarma and Palme (2013).

that this (theoretical) bulk composition also falls within, or close to, the low-temperature two-liquid field. Thus, unmixing was most likely due to low-temperature liquid immiscibility, yet it remains questionable whether the textures described above show the result of *stable* or *metastable* unmixing. Stable unmixing in laboratory experiments is usually recognized by the presence of large (>10 μm diameter) droplets of one liquid disseminated in the conjugate matrix liquid, whereas metastable unmixing (which is due to insufficient time for crystallization during quenching) results in minute, nm-sized quench droplets (Hess, 1977; Freestone and Powell, 1983). As noted by Philpotts (2008) and demonstrated by Hamann et al. (2015) for impact melts, stable immiscible droplets tend to develop a second set of minute immiscible quench droplets. The silicate inclusions in Netschaëvo show *Lsi* droplets ⩽1.5 μm that show a second set of quench droplets in their cores, quite similar to the *Lsi* phases known from impact melts from the Wabar, Saudi Arabia (Hamann et al., 2013), and Kamil, Egypt (Hamann et al., 2015), impact craters. Hence, it has to be concluded that unmixing—whether stable or metastable—was due to low-temperature liquid immiscibility.

Constraining a temperature at which unmixing could have happened is not as straightforward as recognizing unmixing in the first place. Experimental data on the extent of the stable low-temperature two-liquid field constrain stable melt unmixing to temperatures between 1115 and 1230 °C in the system K_2O–FeO–Al_2O_3–SiO_2 (Roedder, 1978). Therefore we can cautiously define a temperature interval of ~1115 to ~1230 °C for final equilibration of the two melts before solidification of *Lsi* and crystallization of phosphoran olivine and Cl-apatite. This temperature range also provides a minimum temperature for the oxidation of P and Cr in the metallic melt, the redistribution of P and Cr between metal and silicate, and the unmixing of the liquids.

5.4.4. Formation of apatite and phosphoran olivine

Phosphoran olivine and Cl-apatite appear interwoven with each other, indicating they co-precipitated. The typical hopper morphology of the Cl-apatite crystals and the fact that the preservation of phosphoran olivine in the presence of a melt is limited to only a few weeks (Boesenberg and Hewins, 2010) indicates that these phases were formed during very rapid cooling and that the sample was not heated again after their formation. For phosphate saturation, Tollari et al. (2006) experimentally defined an equation to predict the P_2O_5 content of the coexisting silicate liquid:

$$M_{P_2O_5}^{Liq-sat} = \exp\left[T\left(\frac{-0.8579}{139.00 - M_{SiO_2}^{Liq}} + 0.0165\right) - 3.3333\ln(M_{CaO}^{Liq})\right] \quad (4)$$

where M represents the molar percentage of the oxides and T is the temperature in K. Here, we want to deduce a temperature at which Cl-apatite saturated. As discussed previously, Cl-apatite probably precipitated from the *Lfe* melt. Using the average concentration of SiO_2, CaO, and P_2O_5 measured in the SiO_2-poor silico-phosphate melt (Table 1), a temperature of 1150 °C is calculated. This means that quenching occurred near or below 1150 °C. This temperature is based on the average composition and was probably locally higher or lower, depending on the availability of SiO_2, CaO, and P_2O_5 in the melt.

6. IMPLICATIONS

One of the most important observations from this study is the high amount of phosphorus in the outer parts of the silicate inclusion, situated close to the metal host. This indicates that phosphorus, originally contained in the metal host of Netschaëvo, re-partitions into the silicate melt upon cooling. In other meteorite groups, such as the IIIAB irons, this process was responsible for the presence of oxide phases, formed as a consequence of oxygen build-up in the metallic liquid during cooling and fractional crystallization. In silicate-free irons, the lack of a lithophile component results in a peculiar Fe–Mn phosphate mineralogy with no phosphoran olivine (Olsen et al., 1999). In contrast, oxidation processes were responsible for the conspicuous mineralogies of the stony-iron pallasite achondrites (Boesenberg et al., 2012; McKibbin and Claeys 2014; Fowler-Gerace and Tait, 2015; McKibbin et al., 2015, 2016), which consist mainly of olivine and metal and are thought to have formed by mixing of mantle and core material (*e.g.*, Buseck, 1977). Like in Netschaëvo, phosphoran olivine is present in some pallasite meteorites, where it crystallized from a P_2O_5-rich silicate liquid (Boesenberg and Hewins, 2010). Apart from phosphoran olivine, at least four primary (probably igneous or metamorphic) phosphate minerals are present in pallasites: merrillite [$Ca_{18}Na_2Mg_2(PO_4)_2$], stanfieldite [$Ca_3Mg_3(PO_4)_4$], farringtonite [$Mg_3(PO_4)_2$], and a silico-phosphate (summarized in Boesenberg et al., 2012). These phosphates can be divided into two groups based on their REE pattern: one that has low REE concentrations and is enriched in HREE and one that has high REE concentrations, is enriched in LREE, and has negative europium anomalies (Davis and Olsen, 1991). This probably indicates that two different processes were responsible for their formation, such as a near- or possibly slightly sub-solidus oxidation reaction for the first group and formation from a melt for the second group (Boesenberg et al., 2012). It should, however, be noted that these magmatic processes are distinct from the far sub-solidus (~700 °C and below) kamacite–taenite exsolution and inferred slow cooling rates, which occurred after magmatic evolution ceased (Yang et al., 2010). The presence of these near-solidus crystallizing phases rich in phosphorus, present in pallasites (from more than one parent body: Davis and Olsen, 1991; Hutcheon and Olsen, 1991) and in this study, indicates that re-partitioning of phosphorus might be a general process in planetesimal core–mantle environments. Thus, the Netschaëvo sample might serve as a natural planetesimal core–mantle boundary experiment and can be used to constrain the temperature range over which phosphorus oxidation and re-partitioning takes place during planetesimal evolution. In the previous sections, we have provided estimates for several processes taking place in the formation of Netschaëvo. It is clear that phosphorus

re-partitioning must have taken place after the crystallization of olivine and before the formation of immiscible melts. From our temperature estimates, this takes place between ~1400–1350 °C and ~1230–1115 °C.

7. CONCLUSIONS

The examined impact melt rock of Netschaëvo contains fine-grained matrix material of quasi-basaltic composition in the inner part of the inclusions, evolving towards a silico-phosphate matrix towards the contact with the metal host. A detailed nano-analytical investigation of the glassy silico-phosphate matrix material of Netschaëvo IIE by FIB-TEM shows that this material consists of phase-separated glass, phosphoran olivine, and quenched Cl-apatite. The presence of Si-rich amorphous globules containing finely-dispersed secondary droplets, as well as textures resembling emulsions formed by spinodal decomposition, indicate the action of silicate liquid immiscibility. Although this has been observed in several terrestrial impact melts, the investigated sample of Netschaëvo constitutes the first clear evidence of silicate liquid immiscibility in meteorites. Several processes took place during cooling of the silicate–metal assemblage, probably occurring in the following order: (i) precipitation of olivine from the liquid, (ii) re-partitioning of phosphorus from the metal into the silicate phase, (iii) formation of immiscible melts, and (iv) crystallization of phosphoran olivine and Cl-apatite in a late quenching event. Re-partitioning of phosphorus from the metal into the silicate phase is a process that probably also took place in pallasite meteorites. These silicate–metal meteorites also contain several late-crystallizing, P-bearing phases and are formed in a core–mantle environment on several parent bodies, indicating that re-partitioning of phosphorus could be a general process in these environments. By means of the Netschaëvo sample, providing a natural planetesimal core–mantle boundary experiment, the temperature at which this process takes place is estimated. Based on temperature ranges defined for olivine precipitation and the formation of immiscible melts, oxidation of phosphorus and re-partitioning must have occurred between ~1400–1350 °C and ~1230–1115 °C.

ACKNOWLEDGMENTS

We are grateful for the thorough reviews and constructive comments by Alan Rubin and an anonymous reviewer, who greatly helped to improve our manuscript. Moreover, we thank Chris Herd for editorial handling and the Natural History Museum of London for providing the sample of Netschaëvo (registration number: BM.33953). NVR and VD thank the FRS-FNRS for funding through an incentive grant. CH thanks the Barringer Family Fund for a student travel grant and the DFG for funding (MEMIN research unit FOR 887, grant He-2893/8-2). SMcK is a postdoctoral fellow of the Research Foundation Flanders (FWO). PhC thanks the FWO (grants: G.A078.11 & G.0021.11). Skillful FIB preparation by Anja Schreiber (GFZ) is greatly acknowledged, and we thank Peter Czaja (MfN) for assistance at the electron microprobe. This research has partly been funded by the Interuniversity Attraction Poles Program "Planet Topers", initiated by the Belgian Science Policy Office.

APPENDIX A. SUPPLEMENTARY MATERIAL

Supplementary data associated with this article can be found, in the online version, at http://dx.doi.org/10.1016/j.gca.2016.10.042.

REFERENCES

Armstrong J. T., Kennedy A. K., Carpenter P. K. and Albee A. L. (1990) Petrography and trace element chemistry of Colomera (IIE) silicate inclusions: rhyolitic plums in the pudding. *Lunar Planet. Sci. XXI*. Lunar Planet. Inst., Houston. #22(abstr.).

Agrell S. O., Charnley N. R. and Chinner G. A. (1998) Phosphoran olivine from Pine Canyon, Piute Co., Utah. *Mineral. Mag.* **62**, 265–269.

Bargossi G. M., Del Moro A., Ferrari M., Gasparotto G., Mordenti A., Rottura A. and Tateo F. (1999) Caratterizzazione petrografico-geochimica e significato dell'associazione monzo-granito-inclusi femici microgranulari della Vetta di Cima d'Asta (Alpi Meridionali). *Mineral. Petrog. Acta* **42**, 155–179.

Bence A. E. and Burnett D. S. (1969) Chemistry and mineralogy of the silicates and metal of the Kodaikanal meteorite. *Geochim. Cosmochim. Acta* **33**, 387–407.

Bishop F. C., Smith J. V. and Dawson J. B. (1976) Na, P, Ti and coordination of Si in garnet from peridotite and eclogite xenoliths. *Nature* **260**, 696–697.

Boesenberg J. S. (2006) Wrought iron from the USS monitor: mineralogy, petrology and metallography. *Archaeometry* **48**, 613–631.

Boesenberg J. S. and Hewins R. H. (2010) An experimental investigation into the metastable formation of phosphoran olivine and pyroxene. *Geochim. Cosmochim. Acta* **74**, 1923–1941.

Boesenberg J. S., Delaney J. S. and Hewins R. H. (2012) A petrological and chemical reexamination of Main Group pallasite formation. *Geochim. Cosmochim. Acta* **89**, 134–158.

Bogaerts M. and Schmidt M. W. (2006) Experiments on silicate melt immiscibility in the system Fe_2SiO_4–$KAlSi_3O_8$–SiO_2–CaO–MgO–TiO_2–P_2O_5 and implications for natural magmas. *Contrib. Mineral. Petrol.* **152**, 257–274.

Bogard D. D., Garrison D. H. and McCoy T. J. (2000) Chronology and petrology of silicates from IIE iron meteorites: evidence of a complex parent body evolution. *Geochim. Cosmochim. Acta* **64**, 2133–2154.

Bowen N. L. (1928) *The Evolution of the Igneous Rocks*. Princeton University Press, Princeton, N.J.

Buchwald V. F. (1975) *Handbook of Iron Meteorites*. Univ California Press, Berkeley.

Bunch T. E., Keil K. and Olsen E. (1970) Mineralogy and petrology of silicate inclusions in iron meteorites. *Contrib. Mineral. Petrol.* **25**, 240–297.

Burnett D. S. and Wasserburg G. J. (1967) Evidence for the formation of an iron meteorite at 3.8×10^9 years. *Earth Planet. Sci. Lett.* **2**, 137–147.

Buseck P. R. (1977) Pallasite meteorites – mineralogy, petrology, and geochemistry. *Geochim. Cosmochim. Acta* **41**, 711–740.

Buseck P. R. and Clark J. (1984) Zaisho – a pallasite containing pyroxene and phosphoran olivine. *Mineral. Mag.* **48**, 229–235.

Capdevilla R. (1967) Répartition et habitus de l'apatite dans le granite de Neira (Espagne): comparaisons avec des données expérimentales et applications petrogénétiques. *C. R. Acad. Sci. Paris* **264**, 1694–1697.

Casanova I., Graf T. and Marti K. (1995) Discovery of an unmelted H-chondrite inclusion in an iron meteorite. *Science* **268**, 540–542.

Chabot N. L. and Drake M. J. (2000) Crystallization of magmatic iron meteorites: the effects of phosphorus and liquid immiscibility. *Meteorit. Planet. Sci.* **35**, 807–816.

Charlier B. and Grove T. L. (2012) Experiments on liquid immiscibility along tholeiitic liquid lines of descent. *Contrib. Mineral. Petrol.* **164**, 27–44.

Charlier B., Namur O. and Grove T. L. (2013) Compositional and kinetic controls on liquid immiscibility in ferrobasalt–rhyolite volcanic and plutonic series. *Geochim. Cosmochim. Acta* **113**, 79–93.

Charlier B., Namur O., Latypov R. and Tegner C. (2015) *Layered Intrusions*. Springer, Dordrecht.

Choi B.-G., Ouyang X. and Wasson J. T. (1995) Classification and origin of IAB and IIICD iron meteorites. *Geochim. Cosmochim. Acta* **59**, 593–612.

Daly R. A. (1914) *Igneous Rocks and their Origin*. McGraw-Hill, New York.

Davis A. M. and Olsen E. J. (1991) Phosphates in pallasite meteorites as probes of mantle processes in small planetary bodies. *Nature* **353**, 637–640.

Ebert M., Hecht L., Deutsch A. and Kenkmann T. (2013) Chemical modification of projectile residues and target material in a MEMIN cratering experiment. *Meteorit. Planet. Sci.* **48**, 134–149.

Fonseca R. O. C., Campbell I. H., O'Neill H. St. C. and Fitzgerald J. D. (2008) Oxygen solubility and speciation in sulphide-rich mattes. *Geochim. Cosmochim. Acta* **72**, 2619–2635.

Fowler-Gerace N. A. and Tait K. T. (2015) Phosphoran olivine overgrowths: implications for multiple impacts to the Main Group pallasite parent body. *Am. Mineral.* **100**, 2043–2052.

Freestone I. C. and Powell R. (1983) The low temperature field of liquid immiscibility in the system K_2O–Al_2O_3–FeO–SiO_2 with special reference to the join fayalite–leucite–silica. *Contrib. Mineral. Petrol.* **82**, 291–299.

Girault J. (1966) Sur la genèse des cristaux d'apatite des carbonatites d'Oka (Canada). *C. R. Acad. Sci. Paris* **263**, 97–100.

Goldstein J. I., Scott E. R. D. and Chabot N. L. (2009) Iron meteorites: crystallization, thermal history, parent bodies, and origin. *Chem. Erde* **69**, 293–325.

Goodrich C. A. (1984) Phosphoran pyroxene and olivine in silicate inclusions in natural iron–carbon alloy, Disko island, Greenland. *Geochim. Cosmochim. Acta* **48**, 1115–1126.

Goodrich C. A. (2003) Petrogenesis of olivine-phyric shergottites Sayh al Uhaymir 005 and Elephant Moraine A79001 lithology A. *Geochim. Cosmochim. Acta* **67**, 3735–3771.

Haack H. and McCoy T. J. (2004) Iron and stony-iron meteorites. In *Treatise on Geochemistry (vol.1): Meteorites, Comets and Planets* (ed. A. M. Davis). Elsevier, pp. 325–345.

Hamann C., Hecht L., Ebert M. and Wirth R. (2013) Chemical projectile–target interaction and liquid immiscibility in impact glass from the Wabar craters, Saudi Arabia. *Geochim. Cosmochim. Acta* **121**, 291–310.

Hamann C., Fazio A., Schultze D., Ebert M., Hecht L., Reimold W. U. and Wirth R. (2015). Silicate liquid immiscibility in natural and experimental impact melts. *Lunar Planet. Sci. XLVI*. Lunar Planet. Inst., Houston. #2071(abstr.).

Hamann C., Luther R., Ebert M., Hecht L., Deutsch A., Wünnemann K., Schäffer S., Osterholz J. and Lexow B. (2016) Correlating laser-generated melts with impact-generated melts: an integrated thermodynamic-petrologic approach. *Geophys. Res. Lett.* **43**, 10602–10610.

Hess P. C. (1977) Structure of silicate melts. *Can. Mineral.* **15**, 162–178.

Hsu W. (2003) Rare earth element geochemistry and petrogenesis of Miles (IIE) silicate inclusions. *Geochim. Cosmochim. Acta* **67**, 4807–4821.

Hudon P. and Baker D. R. (2002) The nature of phase separation in binary oxide melts and glasses. I. silicate systems. *J. Non-Cryst. Solids* **303**, 299–345.

Hutcheon I. and Olsen E. (1991) Cr isotopic composition of differentiated meteorites: a search for 53 Mn. *Lunar Planet. Sci. XXII*. Lunar Planet. Inst., Houston. #605(abstr.).

Ikeda Y. and Prinz M. (1996) Petrology of silicate inclusions in the Miles IIE iron. *Proc. NIPR Symp. Antarct. Meteorit.* **9**, 143–173.

Ikeda Y., Ebihara M. and Prinz M. (1997) Petrology and chemistry of the Miles IIE iron. I: description and petrology of twenty new silicate inclusions. *Antarctic Meteorit. Res.* **10**, 355–372.

Jakobsen J. K., Veksler I. V., Tegner C. and Brooks C. K. (2005) Immiscible iron- and silica-rich melts in basalt petrogenesis documented in the Skaergaard intrusion. *Geology* **33**, 885–888.

Jana D. and Walker D. (1997a) The influence of silicate melt composition on distribution of siderophile elements among metal and silicate liquids. *Earth Planet. Sci. Lett.* **150**, 463–472.

Jana D. and Walker D. (1997b) The influence of sulfur on partitioning of siderophile elements. *Geochim. Cosmochim. Acta* **61**, 5255–5277.

James P. F. (1975) Liquid-phase separation in glass-forming systems. *J. Mater. Sci.* **10**, 1802–1825.

Kracher A. (1983) Notes on the evolution of the IIIAB/pallasite parent body. *Lunar Planet Sci. XIV*. Lunar Planet. Inst., Houston. #405(abstr.).

McCoy T. J. (1995) Silicate-bearing IIE irons: early mixing and differentiation in a core mantle environment and shock resetting of ages. *Meteoritics* **30**, 542–543.

McKibbin S. J. and Claeys P. (2014). Heterogeneous, rapid crystallization of the Main-Group pallasite parent body: planetesimal history from principle component analysis of metal geochemistry and accessory phase mineralogies. *Papers Presented to the 37th Symposium on Antarctic Meteorites*. National Institute of Polar Research, Tokyo.

McKibbin S. J., Pittarello L. and Claeys P. (2015). Contrasting styles of interaction between core and mantle reservoirs in the Main-group pallasite source. *25th Goldschmidt Conference*. Prague Congress Center, Prague. #2079(abstr.).

McKibbin S. J., Ireland T. R., Holden P., O'Neill H. St. C. and Mallmann G. (2016) Rapid cooling of planetesimal core–mantle reaction zones from Mn–Cr isotopes in pallasites. *Geochem. Persp. Lett.* **2**, 68–77.

Mittlefehldt D. W., McCoy T. J., Goodrich C. A. and Kracher A. (1998) Non-chondritic meteorites from asteroidal bodies. In *Planetary Materials*, vol. 36 (ed. J. J. Papike), pp. 4.1–4.195. Reviews in Mineralogy and Geochemistry.

Mysen B. and Richet P. (2005) *Silicate Glasses and Melts*. Elsevier, Amsterdam.

Newsom H. E. and Drake M. J. (1983) Experimental investigations of the partitioning of phosphorus between metal and silicate phases: implications for the Earth, Moon and eucrite parent body. *Geochim. Cosmochim. Acta* **47**, 93–100.

Olsen E. and Jarosewich E. (1971) Chondrules: first occurence in an iron meteorite. *Science* **174**, 583–585.

Olsen E., Davis A., Clarke R. S. J., Schultz L., Weber H. W., Clayton R., Mayeda T., Jarosewich E., Sylvester P., Grossman L., Wang M.-S., Lipschutz M. E., Steele I. M. and Schwade J. (1994) Watson: a new link in the IIE iron chain. *Meteoritics* **29**, 200–213.

Olsen E., Kracher A., Davis A. M., Steele I. M., Hutcheon I. D. and Bunch T. E. (1999) The phosphates of IIIAB iron meteorites. *Meteorit. Planet. Sci.* **34**, 285–300.

Osadchii E. G., Baryshnikova G. V. and Novikov G. V. (1981) The Elga meteorite: silicate inclusions and shock metamorphism. *Proc. Lunar Planet. Sci* **12B**, 1049–1068.

Pak J. J. and Fruehan R. J. (1986) Soda slag system for hot metal dephosphorization. *Met. Trans.* **17B**, 797–804.

Piccoli P. M. and Candela P. (2002) Apatite in igneous systems. In *Phosphates; Geochemical, Geobiological, and Materials Importance*, vol. 48 (eds. M. L. Kohn, J. Rakovan and J. M. Hughes), pp. 255–292. Reviews in Mineralogy and Geochemistry.

Philpotts A. R. (1982) Composition of immiscible liquids in volcanic rocks. *Contrib. Mineral. Petrol.* **80**, 201–218.

Philpotts A. R. (2008) Comment on: liquid immiscibility and the evolution of basaltic magma. *J. Petrol.* **49**, 2171–2175.

Prinz M., Nehru C. E. and Delaney J. S. (1982) Sombrerete: an iron with highly fractionated amphibole-bearing Na–P silicate inclusions. *Lunar Planet. Sci. XIII*. Lunar Planet. Inst., Houston. #634(abstr.).

Prinz M., Nehru C. E., Delaney J. S., Weisberg M., Olsen E. (1983) Globular silicate inclusions in IIE irons and Sombrerete: highly fractionated minimum melts. *Lunar Planet. Sci. XIV*. Lunar Planet. Inst., Houston. #618(abstr.).

Putirka K. D. (2005) Mantle potential temperatures at Hawaii, Iceland, and the mid-ocean ridge system, as inferred from olivine phenocrysts: evidence for thermally driven mantle plumes. *Geochem. Geophys. Geosyst.* **6**, 1–14.

Righter K. and Drake M. J. (2000) Metal/silicate equilibrium in the early Earth: new constraints from the volatile moderately siderophile elements Ga, Cu, P and Sn. *Geochim. Cosmochim. Acta* **64**, 3581–3597.

Righter K., Pando K. M., Danielson L. and Lee C.-T. (2010) Partitioning of Mo, P and other siderophile elements (Cu, Ga, Sn, Ni, Co, Cr, Mn, V, and W) between metal and silicate melt as a function of temperature and silicate melt composition. *Earth Planet. Sci. Lett.* **291**, 1–9.

Roedder E. (1978) Silicate liquid immiscibility in magmas and in the system K_2O–FeO–Al_2O_3–SiO_2: an example of serendipity. *Geochim. Cosmochim. Acta* **42**, 1597–1617.

Roedder E. (1979) Silicate liquid immiscibility in magmas. In *The Evolution of the Igneous Rocks* (ed. , Jr.H. S. Yoder). Princeton University Press, pp. 15–57.

Roedder E. and Weiblen P. W. (1970) Lunar petrology of silicate melt inclusions, Apollo 11 rocks. *Proc. Apollo 11 Lunar Sci. Conf., Geochim. Cosmochim. Acta* **1**(1), 801–837.

Roedder E. and Weiblen P. W. (1971) Petrology of silicate melt inclusions, Apollo 11 and Apollo 12 and terrestrial equivalents. *Proc. 2nd Lunar Sci. Conf.* **1**, 507–528.

Roeder P. L. and Emslie R. F. (1970) Olivine liquid equilibrium. *Contrib. Mineral. Petrol.* **29**, 275–289.

Rubin A. E., Jerde E. A., Zong P., Wasson J. T., Westcott J. W., Mayeda T. K. and Clayton R. N. (1986) Properties of the Guin ungrouped iron meteorite: the origin of Guin and of group-IIE irons. *Earth Planet. Sci. Lett.* **76**, 209–226.

Ruzicka A. M. (2014) Silicate-bearing iron meteorites and their implications for the evolution of asteroidal parent bodies. *Chem. Erde-Geochem.* **74**, 3–48.

Ruzicka A. M. and Hutson M. (2010) Comparative petrology of silicates in the Udei Station (IAB) and Miles (IIE) iron meteorites: implications for the origin of silicate-bearing irons. *Geochim. Cosmochim. Acta* **74**, 394–433.

Ruzicka A. M., Boynton W. and Ganguly J. (1994) Olivine coronas, metamorphism, and the thermal history of the Morristown and Emery mesosiderites. *Geochim. Cosmochim. Acta* **58**, 2725–2741.

Ruzicka A. M., Fowler G. W., Snyder G. A., Prinz M., Papike J. J. and Taylor L. A. (1999) Petrogenesis of silicate inclusions in the Weekeroo Station IIE iron meteorite: differentiation, remelting, and dynamic mixing. *Geochim. Cosmochim. Acta* **63**, 2123–2143.

Ruzicka A. M., Hutson M. and Floss C. (2006) Petrology of silicate inclusions in the Sombrerete ungrouped iron meteorite: implications for the origins of IIE-type silicate-bearing irons. *Meteorit. Planet. Sci.* **41**, 1797–1831.

Schmitt W., Palme H. and Wanke H. (1989) Experimental determination of metal/silicate partition coefficients for P, Co, Ni, Cu, Ga, Ge, Mo, W and some implications for the early evolution of the Earth. *Geochim. Cosmochim. Acta* **53**, 173–186.

Scott E. R. D. (1972) Chemical fractionation in iron meteorites and its interpretation. *Geochim. Cosmochim. Acta* **36**, 1205–1236.

Scott E. R. D. and Wasson J. T. (1976) Chemical classification of iron meteorites – VIII. Groups IC, IIE, IIIF and 97 other irons. *Geochim. Cosmochim. Acta* **40**, 103–115.

Sensarma S. and Palme H. (2013) Silicale liquid immiscibility in the ~2.5 Ga Fe-rich andesite at the top of the Dongargarh large igneous province (India). *Lithos* **170–171**, 239–251.

Shelby J. E. (2005) *Introduction to Glass Science and Technology*. The Royal Society of Chemistry, Cambridge.

Takeda H., Hsu W. and Huss G. R. (2003) Mineralogy of silicate inclusions of the Colomera IIE iron and crystallization of Cr-diopside and alkali feldspar from a partial melt. *Geochim. Cosmochim. Acta* **67**, 2269–2288.

Thompson R. N. (1975) Is upper-mantle phosphorus contained in sodic garnet? *Earth Planet Sci. Lett.* **26**, 417–424.

Tollari N., Toplis M. J. and Barnes S.-J. (2006) Predicting phosphate saturation in silicate magmas: an experimental study of the effects of melt composition and temperature. *Geochim. Cosmochim. Acta* **70**, 1518–1536.

Tollari N., Baker D. R. and Barnes S.-J. (2008) Experimental effects of pressure and fluorine on apatite saturation in mafic magmas, with reference to layered intrusions and massif anorthosites. *Contrib. Mineral. Petrol.* **156**, 161–175.

Toplis M. J., Dingwell D. B. and Libourel G. (1994) The effect of phosphorus on the iron redox ratio, viscosity and density of an evolved ferro-basalt. *Contrib. Mineral. Petrol.* **117**, 293–304.

Tropper P., Recheis A. and Konzett J. (2004) Pyrometamorphic formation of phosphorous-rich olivines in partially molten metapelitic gneisses from a prehistoric sacrificial burning site (Otz valley, Tyrol, Austria). *Eur. J. Mineral.* **16**, 631–640.

Ulff-Møller F. (1985) Solidification history of the Kitdlit lens: immiscible metal and sulfide liquids from a basaltic dike on Disko, Central West Greenland. *J. Petrol.* **26**, 64–91.

Ulff-Møller F. (1998) Solubility of chromium and oxygen in metallic liquids and the co-crystallization of chromite and metal in iron meteorite parent bodies. *Lunar Planet. Sci. XXIX*. Lunar Planet. Inst., Houston. #1969(abstr.).

Usui T., Jones J. and Mittlefehldt D. W. (2015) A partial melting study of an ordinary (H) chondrite composition with application to the unique achondrite Graves Nunataks 06128 and 06129. *Meteorit. Planet. Sci.* **50**, 759–781.

Van Roosbroek N., Debaille V., Pittarello L., Goderis S., Humayun M., Hecht L., Jourdan F., Spicuzza M., Vanhaecke F. and Claeys Ph. (2015) The formation of IIE iron meteorites investigated by the chondrule-bearing Mont Dieu meteorite. *Meteorit. Planet. Sci.* **50**, 1173–1196.

Van Roosbroek N., Pittarello L., Greshake A., Debaille V. and Claeys Ph. (2016) First finding of impact melt in the IIE Netschaëvo meteorite. *Meteorit. Planet. Sci.* **51**, 372–389.

Veksler I. V., Dorfman A. M., Borisov A. A., Wirth R. and Dingwell D. B. (2007) Liquid immiscibility and the evolution of basaltic magma. *J. Petrol.* **48**, 2187–2210.

Veksler I. V., Dorfman A. M., Rhede D., Wirth R., Borisov A. A. and Dingwell D. B. (2008) Liquid unmixing kinetics and the extent of immiscibility in the system K_2O–CaO–FeO–Al_2O_3–SiO_2. *Chem. Geol.* **256**, 119–130.

Wang Y., Hua X. and Hsu W. (2006). Phosphoran-olivine in opaque assemblages of the Ningqiang carbonaceous chondrite: implication to their precursors. *Lunar Planet. Sci. XXXVII.* Lunar Planet Inst., Houston. #1504(abstr.).

Wasserburg G. J., Sanz G. J. and Bence A. E. (1968) Potassium-feldspar phenocrysts in the surface of Colomera, an iron meteorite. *Science* **161**, 684–687.

Wasson J. T. and Wang J. (1986) A nonmagmatic origin of group-IIE iron meteorites. *Geochim. Cosmochim. Acta* **50**, 725–732.

Wasson J. T., Lange D. E., Francis C. A. and Ulff-Moller F. (1999) Massive chromite in the Brenham pallasite and the fractionation of Cr during the crystallization of asteroidal cores. *Geochim. Cosmochim. Acta* **63**, 1219–1232.

Watson E. B. (1979) Apatite saturation in basic to intermediate magmas. *Geophys. Res. Lett.* **6**, 937–940.

Watson E. B. (1980) Apatite and phosphorus in mantle source regions—an experimental study of apatite/melt equilibria at pressures to 25 Kbar. *Earth Planet. Sci. Lett.* **51**, 322–335.

Wirth R. (2009) Focused ion beam (FIB) combined with SEM and TEM: advanced analytical tools for studies of chemical composition, microstructure and crystal structure in geomaterials on a nanometre scale. *Chem. Geol.* **261**, 217–229.

Wood M. I. and Hess P. C. (1980) The structural role of Al_2O_3 and TiO_2 in immiscible silicate liquids in the system SiO_2–MgO–CaO–FeO–TiO_2– Al_2O_3. *Contrib. Mineral. Petrol.* **72**, 319–328.

Wyllie P. J., Cox K. G. and Biggar G. M. (1962) The habit of apatite in synthetic systems and igneous rocks. *J. Petrol.* **3**, 238–243.

Yang J., Goldstein J. I. and Scott E. R. D. (2010) Main-group pallasites: thermal history, relationship to IIIAB irons, and origin. *Geochim. Cosmochim. Acta* **74**, 4471–4492.

Young R. W., Duffy J. A., Hassall G. J. and Xu Z. (1992) Use of optical basicity concept for determining phosphorus and sulphur slag–metal partitions. *Ironmak. Steelmak.* **19**, 201–219.

Zolensky M. E. and Koeberl C. (1991) Why are blue zhamanshinites blue? Liquid immiscibility in an impact melt. *Geochim. Cosmochim. Acta* **55**, 1483–1486.

Associate editor: Chris Herd